

A SPECTROSCOPIC SURVEY OF *WISE*-SELECTED OBSCURED QUASARS WITH THE SOUTHERN AFRICAN LARGE TELESCOPE

KEVIN N. HAINLINE¹, RYAN C. HICKOX¹, CHRISTOPHER M. CARROLL¹, ADAM D. MYERS²,
MICHAEL A. DiPOMPEO², AND LAURA TROUILLE³

¹ Department of Physics and Astronomy, Dartmouth College, Hanover, NH 03755

² Department of Physics and Astronomy, University of Wyoming, Laramie, WY 82071

³ Center for Interdisciplinary Exploration and Research in Astrophysics (CIERA) and Department of Physics and Astronomy, Northwestern University, Evanston, IL 60208, The Adler Planetarium, Chicago, IL 60605

Received 2014 May 21; accepted 2014 September 18; published 2014 October 21

ABSTRACT

We present the results of an optical spectroscopic survey of a sample of 40 candidate obscured quasars identified on the basis of their mid-infrared emission detected by the *Wide-Field Infrared Survey Explorer* (*WISE*). Optical spectra for this survey were obtained using the Robert Stobie Spectrograph on the Southern African Large Telescope. Our sample was selected with *WISE* colors characteristic of active galactic nuclei (AGNs), as well as red optical to mid-IR colors indicating that the optical/UV AGN continuum is obscured by dust. We obtain secure redshifts for the majority of the objects that comprise our sample (35/40), and find that sources that are bright in the *WISE* W4 (22 μ m) band are typically at moderate redshift ($\langle z \rangle = 0.35$) while sources fainter in W4 are at higher redshifts ($\langle z \rangle = 0.73$). The majority of the sources have narrow emission lines with optical colors and emission line ratios of our *WISE*-selected sources that are consistent with the locus of AGN on the rest-frame $g - z$ color versus [Ne III] λ 3869/[O II] λ 3726+3729 line ratio diagnostic diagram. We also use empirical AGN and galaxy templates to model the spectral energy distributions (SEDs) for the objects in our sample, and find that while there is significant variation in the observed SEDs for these objects, the majority require a strong AGN component. Finally, we use the results from our analysis of the optical spectra and the SEDs to compare our selection criteria to alternate criteria presented in the literature. These results verify the efficacy of selecting luminous obscured AGNs based on their *WISE* colors.

Key words: galaxies: active – galaxies: nuclei

Online-only material: color figures

1. INTRODUCTION

A complete understanding of the evolution of galaxies requires a detailed exploration of the role played by active galactic nuclei (AGNs), highly luminous objects found in the centers of galaxies that are powered by accretion onto a supermassive black hole. The most powerful AGNs, quasars, have been proposed to influence the interstellar gas content and temperature throughout a galaxy, which may lead to reduced star formation (SF; for recent reviews, see Fabian 2012; Alexander & Hickox 2012). The line-of-sight orientation between the central supermassive black hole and any obscuring dust is thought to produce the array of different observed AGNs (Antonucci 1993; Urry & Padovani 1995). This “unification theory” separates AGNs into two broad classes: obscured AGNs, where nuclear and galaxy-scale dust blocks emission from near the central black hole, and unobscured AGNs, where there exists a line of sight down to the central engine. It is far more straightforward to detect unobscured AGNs, while the full population of obscured AGNs is not fully characterized. Historically, unobscured AGNs have been selected by observing broad emission lines emitted from excited gas near the accreting supermassive black hole, and are often called Type I AGNs to differentiate them from Type II AGNs whose spectra only contain narrow emission lines. The difficulty in finding obscured AGNs is important given the evidence for an evolutionary link between obscured and unobscured AGNs. One of the primary proposed methods for fueling a quasar is through major mergers of gas-rich galaxies, where gas is funneled into the central regions of the galaxy (Kauffmann & Haehnelt 2000;

Hopkins et al. 2006, 2008). It is thought that quasar fueling can also lead to an obscuration of the UV and optical emission from the accretion process by the in-falling gas and dust, which would eventually be lifted by quasar radiative feedback, setting up a large-scale connection between the supermassive black hole and galaxy-wide SF (Chen et al. 2014). Understanding the full population of obscured AGNs is vital for exploring both the cosmological growth of supermassive black holes as well as the connection to their host galaxies and larger-scale galaxy environments.

Deep X-ray surveys using both *XMM-Newton* and *Chandra* have revealed extensive samples of AGNs with a wide luminosity range out to large cosmic distances (Mainieri et al. 2002; Alexander et al. 2003; Mateos et al. 2005; Brandt & Alexander 2010; Xue et al. 2011). AGN population synthesis models, however, require a substantial number of obscured AGNs to explain the shape of the cosmic X-ray background spectrum (Comastri et al. 1995; Gilli et al. 2007; Treister et al. 2009; Ballantyne et al. 2011; Shi et al. 2013), and many of these objects have been missed in existing X-ray surveys (Worsley et al. 2005; Tozzi et al. 2006; Alexander et al. 2008; Burlon et al. 2011). A complimentary approach is to target obscured AGNs selected at mid-infrared (mid-IR) wavelengths, where obscuration effects are minimized and reprocessed light from dust near the central supermassive black hole produces a characteristic red IR power-law spectrum. Lacy et al. (2004) and Stern et al. (2005) described robust color criteria for separating AGNs from star-forming galaxies using the IR photometric bands targeted with the Infrared Array Camera (IRAC) instrument on the *Spitzer*

Space Telescope, which was further explored in Donley et al. (2008, 2012) and Mendez et al. (2013). Hickox et al. (2007) studied a large sample of obscured and unobscured objects in the Boötes field selected to be AGNs by their IRAC colors. They demonstrated a bimodality in optical to mid-IR color that they used to separate obscured and unobscured sources. Lacy et al. (2013) presented an optical and near-IR spectroscopic study of a large sample of 786 objects selected with *Spitzer* IRAC colors indicative of AGN activity and demonstrated the power in using *Spitzer* selection techniques to target AGNs and obscured quasars even out to $z \sim 2-3$. However, IRAC-based studies like these are limited to only the relatively small fields observed by *Spitzer*. Recently, the all-sky mid-IR photometric coverage from the *Wide-field Infrared Survey Explorer* (*WISE*; Wright et al. 2010) has also been used by many authors to separate active galaxies from star-forming galaxies. *WISE* covered the entire sky at four wavelengths: 3.4, 4.6, 12, and 22 μm (referred to as *W1*, *W2*, *W3*, and *W4* throughout this work), reaching 5σ point-source sensitivities better than 0.08, 0.11, 1, and 6 mJy in each photometric band, respectively. This unprecedented all-sky coverage makes *WISE* a powerful tool for selecting large numbers of obscured active galaxies for follow-up studies.

There has been a wealth of research into the selection of AGNs by their *WISE* colors. Assef et al. (2010), Ashby et al. (2009), and Stern et al. (2012) described *WISE* selection criteria that use only the *W1*–*W2* color to separate AGNs from star-forming galaxies. Stern et al. (2012) used *WISE* data from the COSMOS field to demonstrate that a *WISE* color cut of $W1 - W2 > 0.8$ is successful at recovering 78% of *Spitzer*-selected AGNs. A less conservative color cut, such as $W1 - W2 > 0.5$ suggested by Ashby et al. (2009), was shown to increase the completeness of the AGN sample, but the recovered sample suffered from more contamination from star-forming galaxies. Mateos et al. (2012) used a mid-IR-selection method which relies on three of the *WISE* photometric bands: *W1*, *W2*, *W3*. Using X-ray selected AGNs from the Bright Ultrahard *XMM-Newton* Survey, the authors demonstrated that the completeness of their MIR-selection method is strongly dependent on AGN luminosity, especially as compared to the luminosity of the host galaxy.

While many of the methods used to define *WISE* obscured AGN selection rely on exploring the *WISE* colors of large existing samples of active galaxies, it would be of interest to test these selection methods using a blind survey of obscured objects selected solely by their colors. By performing follow-up spectroscopy, we can test obscured AGN selection criteria, and explore both the type of objects and the redshift distribution of objects with red IR colors. Surveys of this nature are useful for understanding the full population of *WISE*-selected obscured quasars, as it is necessary to employ the large statistical sample of *WISE* quasars to study spatial clustering (e.g., Donoso et al. 2013, DiPompeo et al. 2014) as well as the role that AGNs play in galaxy evolution. Additionally, the all-sky coverage of *WISE* can be used to target rare objects of which there are few in existing spectroscopic fields.

In this paper, we present long-slit optical spectroscopy obtained with the Southern African Large Telescope (SALT) for a sample of 40 objects selected with *WISE* and Sloan Digital Sky Survey (SDSS) colors indicative of obscured quasar activity. We describe the full sample and our selection criteria in Section 2, examine the optical spectra and redshift distribution for the objects in Section 3, and in Section 4 we discuss the use of various optical emission line diagnostics to examine the physical characteristics of objects that comprise the sample. We present the

results of modeling the spectral energy distributions (SEDs) of the sample with a combination of AGN and star-forming galaxy templates in Section 5. We examine individual objects in our sample in Section 6, compare the selection criteria we used to other recent *WISE* selection criteria in Section 7, and finally, we draw conclusions in Section 8. Throughout, we assume a standard Λ CDM cosmological model with $H_0 = 71 \text{ km s}^{-1} \text{ Mpc}^{-1}$, $\Omega_M = 0.27$, and $\Omega_\Lambda = 0.73$ (Komatsu et al. 2011).

2. QUASAR SAMPLE, OBSERVATIONS AND DATA REDUCTION

The sample described in this paper consists of 40 galaxies observed in three queued campaigns between November of 2012 and March of 2014 (SALT Proposals 2012-2-DC-002, 2013-1-DC-003, 2013-2-DC-003; PI: R. Hickox). For the purposes of exploring *WISE* and SDSS obscured quasar selection criteria, we chose objects in two different ways. In order to ensure maximum visibility with SALT, we restricted our possible targets to $-2^\circ < \text{decl.} < 2^\circ$ for the first campaign, and $-2^\circ < \text{decl.} < 0^\circ$ for the second campaign. Importantly, in both campaigns, all targets have $g < 22.4$ in order to increase the likelihood of obtaining a spectrum with high signal to noise with SALT. We further limit the sample to $g > 20$ to probe higher redshifts and avoid bright objects with existing SDSS spectroscopy. The ramifications of this optical selection criteria are described in Section 3. While the majority of the objects in our sample were chosen for optical followup due to the absence of an existing SDSS spectrum, both J0325–0032⁵ and J0924+0027 were selected so that the SALT spectrum could be compared to the SDSS spectrum, as discussed in Section 3.

Our first selection group consists of all objects with SDSS and *WISE* coverage with *WISE* color $W1 - W2 > 0.7$,⁶ a slightly more relaxed criteria for selecting quasars from what is presented in Stern et al. (2012). In practice, while only one object, J1417+0108, has $W1 - W2 = 0.73$, the rest have $W1 - W2 > 0.8$. In order to select objects with the brightest mid-IR emission, we further restricted the possible candidates to only those objects with $7 \geq W4 \geq 6.5$. These relatively rare IR-bright objects are comparable to the *Spitzer* 24 μm bright objects explored in Lacy et al. (2013). We acquired SALT spectroscopy for 21 objects selected under these criteria, which we refer to as “Group 1.”

For the second campaign, we started with only those objects with SDSS and *WISE* coverage with *WISE* color $W1 - W2 > 0.8$, and $W4 \geq 7.0$. We further selected objects with $r_{\text{AB}} - W2_{\text{AB}} > 3.1$, the criteria introduced in Hickox et al. (2007) that targets obscured quasars. We acquired SALT spectroscopy for 19 objects selected under these criteria, which we refer to as “Group 2.” If we only explore the overlapping range in decl. used in selecting our targets for both Group 1 and Group 2 ($-2^\circ < \text{decl.} < 0^\circ$) across all R.A.s, we find 144 objects qualify as Group 1 objects, while 1270 objects qualify as Group 2 objects, due largely to the relaxation of the *W4* photometry criteria for Group 2. Additionally, in this same decl. range, there are

⁴ The SDSS magnitudes used for selection are the DR9 “model” AB magnitudes.

⁵ We refer to the objects in our sample using shortened names. The full names are given in Table 2.

⁶ Using the *WISE* ext_flg value, 39 objects are unresolved in the *WISE* photometry, and for these we use the “profile-fitting” photometric magnitudes taken from the *WISE* All-Sky Source Catalog. For J1609–0004, we use the “standard” aperture magnitudes. For any other samples discussed in this paper, we use the corresponding magnitudes based on the ext_flg values. All *WISE* photometry is given in Vega magnitudes, unless specified.

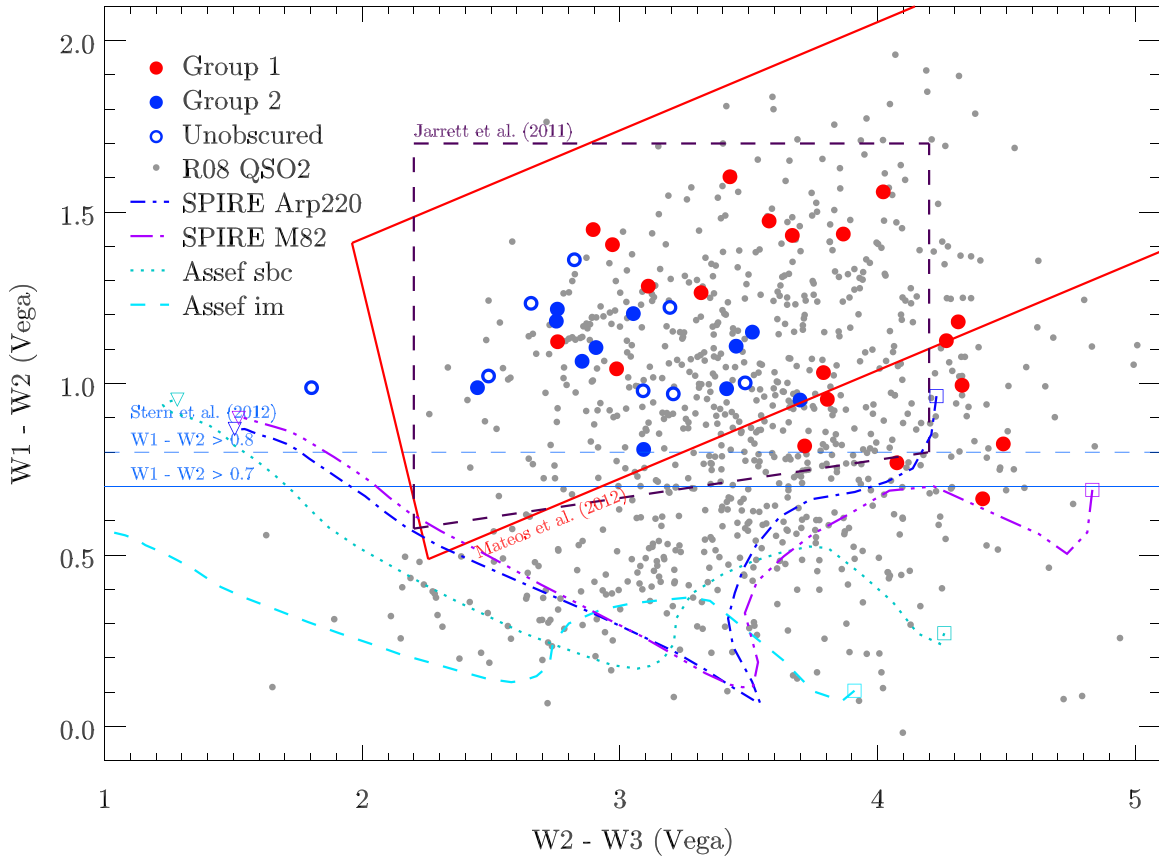


Figure 1. Plot showing *WISE* $W1-W2$ color against $W2-W3$ color. The objects in our SALT sample (as measured with updated AllWISE photometry) are plotted with red (Group 1) and blue (Group 2) circles, and Type II quasars from Reyes et al. (2008) are shown with small light gray circles. Open circles are used to plot objects where the SED modeling (outlined in Section 5) indicates that they are unobscured in the optical. We also plot various AGN selection criteria from the literature. We plot the AGN selection box described in Jarrett et al. (2011) with a purple dashed line, we plot both the $W1-W3$ color cuts described in Stern et al. (2012) with blue solid and dashed horizontal lines, and finally we plot the AGN-selection wedge from Mateos et al. (2012) with a red solid line. While the bulk of our sample fall into the AGN selection regions, individual objects lie outside the different regions. We explore this in more detail in Section 7. To demonstrate the *WISE* colors of star-forming galaxies as a function of redshift, we plot tracks showing how the *WISE* colors for the Assef et al. (2010) Sbc (cyan dotted line), Im (cyan dashed line), and Polletta et al. (2007) Arp220 (blue dot-dashed line) and M82 (purple triple-dot dashed line) templates change as a function of redshift, where $z = 0$ is represented by an open square, and $z = 2$ is represented by an open downward-facing triangle. The most extreme star-forming galaxy M82 does move above the Stern et al. (2012) demarcation at low redshifts.

(A color version of this figure is available in the online journal.)

77 objects that would be selected as Group 1 objects with $g > 22$, while there would be 8166 Group 2 objects with $g > 22$, which represents a significant number of candidate obscured quasars that are missed due to our optical photometric cuts. For the full decl. range used to find Group 1 objects ($-2^\circ < \text{decl.} < 2^\circ$), there are 277 objects that would be selected under the Group 1 criteria, while an additional 145 objects would be selected under these criteria but with $g > 22$.

We plot the *WISE* $W1-W2$ and $W2-W3$ colors for both objects in both Group 1 and 2 in Figure 1 along with AGN selection criteria taken from the literature. We also plot the SDSS-selected Type II quasars (with *WISE* $W1$, $W2$, and $W3$ detections with signal-to-noise ratio (S/N) > 3.0) from Reyes et al. (2008) for comparison. The objects in our sample cover a wide range in colors. To indicate the *WISE* colors of star-forming galaxies as a function of redshift from $z = 0-2$, we also plot tracks showing the Assef et al. (2010) star-forming (“Sbc”) and irregular (“Im”) templates, as well as SEDs for the star-forming galaxies M82 and Arp220 from Polletta et al. (2007). We further discuss the implications of our selection criteria in Section 7. The objects in our sample do not have *Chandra* coverage with any instrument, and while there is *XMM-Newton* coverage for fields containing the objects J1505+0134

and J1129+0102,⁷ the objects were not detected. We also note that 8 of our 45 objects have detections within $2''$ in the Very Large Array (VLA) Faint Images of the Radio Sky at Twenty-Centimeters (FIRST) survey (Becker et al. 1995): J1007+0146 (1.27 mJy integrated 21cm flux, 1.24 mJy beam⁻¹ peak flux), J0852+0137 (3.96 mJy, 3.59 mJy beam⁻¹), J0957-0120 (2.78 mJy, 2.20 mJy beam⁻¹), J1151-0046 (2.85 mJy, 3.16 mJy beam⁻¹), J1333-0126 (1.25 mJy, 1.51 mJy beam⁻¹), J1406-0049 (3.20 mJy, 3.16 mJy beam⁻¹), J1417+0108 (1.38 mJy, 1.64 mJy beam⁻¹), and J1554+0011 (6.15 mJy, 5.78 mJy beam⁻¹). These detections could be caused by both SF as well as AGN activity (Ivezić et al. 2002).

The objects were selected using photometry from SDSS Data Release 9 (Ahn et al. 2012) as well as the *WISE* All-Sky Source Catalog. Recently, the *WISE* team released the AllWISE Source Catalog (Cutri 2013, made public 2013 November), which combined three *WISE* surveys: the 4-band Cryogenic Survey (the primary *WISE* mission that covered the full sky 1.2 times between 2010 January and August), the 3-band Cryogenic

⁷ The *XMM-Newton* observations are Obs-ID:0021540101 (30 ks), 0021540501 (20 ks), 0723800101 (82 ks), and 0723800201 (89 ks) for the field containing J1505+0134, and Obs-ID: 0305750601 (6 ks) for the field containing J1129+0102.

Table 1
Sample Photometric Properties

SDSS Name	Group	SDSS Photometry ^a					WISE Photometry ^b				W1–W2	$r - W_{2AB}$
		u	g	r	i	z	W1	W2	W3	W4		
J032533.31–003216.4	1	21.92	20.79	19.64	19.56	18.98	14.59	12.98	9.56	6.66	1.60	3.32
J033820.71–004935.6	2	21.71	20.89	20.15	19.69	19.34	14.98	13.76	10.56	7.78	1.22	3.05
J035726.82–002724.9	2	21.60	20.84	20.44	19.96	19.73	14.94	13.96	10.87	8.39	0.98	3.14
J073745.20–005229.8	2	21.78	20.17	22.46	19.84	19.13	15.97	15.00	11.79	...	0.97	4.12
J085259.35+013715.1	1	21.62	20.47	19.10	19.20	18.55	15.47	14.48	10.15	6.94	1.00	1.29
J092435.55+002716.4	1	21.91	21.41	20.32	19.46	18.87	13.18	12.06	9.30	6.81	1.12	4.92
J095718.06–012049.1	2	24.63	21.97	20.54	19.90	19.14	14.99	13.88	10.43	8.18	1.11	3.32
J100346.93–011015.9	1	22.95	21.91	20.90	20.38	19.41	14.25	12.99	9.67	6.95	1.27	4.57
J100711.52+014627.1	1	22.46	20.21	19.31	18.76	18.55	14.47	13.00	9.42	6.96	1.47	2.97
J110722.11+013336.8	1	23.51	21.60	19.96	19.30	18.82	14.69	13.74	9.93	6.89	0.95	2.88
J112931.47+010254.7	1	21.63	20.58	19.37	19.05	18.65	14.27	12.84	9.17	6.43	1.43	3.19
J113635.48+015252.9	1	22.25	20.85	19.62	18.84	18.43	13.63	12.58	9.60	6.93	1.04	3.70
J115158.63–004641.2	1	22.00	20.15	19.25	18.86	18.67	15.20	13.76	9.90	7.15	1.44	2.15
J125521.24–001018.2	1	21.65	20.56	19.33	18.94	18.44	15.01	13.97	10.18	7.00	1.03	2.02
J130500.31+005422.1	1	20.89	20.21	19.32	18.97	18.57	15.10	14.27	9.78	6.57	0.82	1.71
J130845.53+015542.0	1	22.35	21.35	20.12	19.88	19.40	13.43	11.99	9.09	6.88	1.45	4.80
J132031.04–010248.3	2	22.98	20.78	19.83	19.46	19.06	13.87	12.63	9.97	7.65	1.23	3.86
J132648.81–003757.6	2	22.23	21.54	21.32	21.10	20.53	15.77	14.82	11.12	...	0.95	3.16
J133331.15–012653.3	1	21.53	20.41	19.29	18.63	18.38	14.88	14.11	10.04	6.66	0.77	1.84
J135423.71–000314.5	1	21.88	21.13	20.55	20.43	19.82	17.54	16.46	10.22	6.97	1.08	0.76
J135534.66–002206.1	2	22.79	21.02	19.62	19.09	18.28	13.15	12.16	9.72	7.53	0.99	4.12
J140618.16–004923.1	2	22.01	20.99	19.49	18.97	18.58	14.15	12.95	9.89	7.06	1.20	3.21
J140830.13–005001.6	2	22.83	21.93	20.65	19.73	19.24	13.97	12.79	10.04	8.08	1.18	4.52
J141724.04+010843.1	1	21.08	20.40	19.73	19.17	18.75	14.87	14.21	9.80	6.58	0.66	2.18
J143459.27–014432.8	1	21.95	20.40	19.40	18.82	18.48	15.20	14.02	9.71	6.62	1.18	2.04
J144006.46–011624.7	1	21.36	20.33	19.24	18.84	18.43	13.69	12.40	9.29	6.78	1.28	3.50
J144625.94–015721.9	2	22.18	21.50	20.46	19.94	19.45	14.11	13.30	10.21	8.24	0.81	3.82
J150539.97+013433.9	1	21.69	20.44	19.28	18.88	18.54	15.02	13.89	9.62	6.93	1.13	2.05
J152736.35–001007.7	2	21.02	20.89	20.12	19.85	18.90	14.44	13.45	11.65	...	0.99	3.33
J153846.30+012951.9	1	23.55	21.25	20.25	19.39	19.35	15.13	13.57	9.55	6.89	1.56	3.34
J154503.94–010010.4	1	21.67	20.86	19.38	18.70	18.43	13.51	12.10	9.13	6.80	1.41	3.94
J155421.94+001115.0	1	22.72	21.09	19.92	18.85	18.54	14.49	13.67	9.95	6.69	0.82	2.91
J160903.75–000426.2	2	22.65	20.99	20.12	19.63	19.18	14.88	13.73	10.22	...	1.15	3.05
J160928.56–013344.1	2	25.86	21.62	20.09	19.29	18.73	14.56	13.57	10.16	7.70	0.99	3.18
J163445.76–010808.6	2	21.01	20.46	20.15	19.76	19.52	14.41	13.39	10.90	...	1.02	3.42
J172446.04–003833.4	2	21.74	20.62	19.48	19.00	18.26	13.45	12.39	9.54	7.16	1.07	3.75
J173114.67–003708.1	2	22.09	21.25	24.81	24.37	20.05	16.12	14.90	12.14	...	1.22	6.57
J180853.93–001650.6	2	21.53	20.65	19.88	19.52	19.26	14.14	13.04	10.13	7.61	1.11	3.50
J194745.03–003603.8	2	22.76	21.73	21.20	20.98	20.33	15.42	14.42	10.93	8.31	1.00	3.44
J202952.16–010805.3	2	21.89	21.02	20.08	19.51	19.26	14.67	13.31	10.48	...	1.36	3.44

Notes.^a DR9 “model” AB magnitudes.^b Where the *WISE* ext_flg value indicates that the objects are unresolved, we use the “profile-fitting” magnitudes (*w*mp*ro). For those where the object is resolved, we use the “standard” aperture magnitudes (*w*mag*). In both cases, the photometry is given in Vega magnitudes.

Survey (a survey using only the first three *WISE* wavebands, which covered 30% of the sky between 2010 January and August), and the NEO-*WISE* post-cryogenic survey (a survey using the first two *WISE* wavebands, which covered 70% of the sky between 2010 September and 2011 February). Most importantly for the purposes of the current study, the AllWISE Data includes updated photometry more sensitive in the W1 and W2 bands, with updated 5σ point-source sensitivities at 0.054 and 0.071 mJy, respectively (Cutri 2013). For the remainder of this paper, we will report the updated, more accurate AllWISE photometry for the objects in our sample. The average fluxes in the W1 and W2 band for the full selection of objects are 600 and 900 μ Jy, respectively. For the majority of the objects, the updated AllWISE photometry does not affect whether or not these objects would be selected, although there are a few objects which would move into or out of our selection boxes. The Group

1 object J1417+0108 has updated photometry with *WISE* color $W1-W2 < 0.7$, which does not satisfy our initial color cut. Similarly, the Group 1 objects J1151–0046 and J1129+0102 have W4-band photometry that excludes them from selection under Group 1 criteria. Finally, J0338–0049 and J1609–0004, two Group 2 objects, have updated color $r_{AB} - W_{2AB} < 3.1$. We further discuss these targets in Section 6. For the W1, W2, and W3 photometry used in our selection, all but one of our objects has AllWISE S/N on the photometry above 3.0 (J1609–0004 has $S/N_{W1} = 2.9$). We only use the observed photometry in the W4 band if the object was observed with $S/N > 3.0$. We report the object identifiers, group number, SDSS and *WISE* AllWISE Source Catalogue photometry, and the IR and optical-to-IR colors used to select the objects in Table 1.

In order to better explore how the change in the *WISE* photometry affected the selection of targets, we explored all

of the objects that would be selected as Group 1 and Group 2 objects in the range $40^\circ < \text{R.A.} < 185^\circ$, $-2^\circ < \text{decl.} < 0^\circ$ with both *WISE* All-Sky and AllWISE photometry. For Group 1, 49 total objects would be selected using both the All-Sky and AllWISE photometry, and an additional five objects moved into the selection criteria and 14 moved out of the selection criteria based on the updated AllWISE photometry, primarily because of updated AllWISE photometry with $W4 > 7$ or $W4 < 6.5$ for individual objects. For Group 2, 323 total objects would be selected using both the *WISE* All-Sky and AllWISE photometry, and an additional 56 objects moved into the selection criteria and 28 moved out of the selection criteria based on the updated AllWISE photometry, due to the larger number of criteria used for selecting an object in Group 2. These results demonstrate the increased sensitivity of the updated AllWISE data, and we reiterate that except where noted above, the objects in our sample would be selected to be a part of Group 1 or Group 2 using either the AllWISE or *WISE* All-Sky photometry.

The full sample of objects were observed using the Robert Stobie Spectrograph (RSS; Kobulnicky et al. 2003; Smith et al. 2006) on SALT in long-slit mode, with a $1''.5$ slit and the PG0900 grating, which provides a spectral resolution of 5 \AA at a central wavelength of 5000 \AA (in this observational set-up, the spectral range was $3600\text{--}6000 \text{ \AA}$). The seeing was measured using stars observed in the acquisition images taken just before the observations, and was typically $\sim 2''$ for the runs. The slit positions were chosen to coincide with a nearby bright source for ease of object acquisition. While the majority of the objects comprising the sample were observed for 2250 s, for a small number of objects with brighter or dimmer optical photometry, the exposure time was changed accordingly, leading to a full range of observing times between 1950 and 3000 s. Data reduction was performed using standard IRAF scripts.⁸ The data were gain-corrected, bias-corrected, and mosaicked with the SALT reduction pipeline. We subsequently flat-fielded the data, applied a wavelength solution using arc lamp spectra, and then used the three observations made for each target for cosmic ray removal. In our final step, the two-dimensional spectra were background subtracted and combined using a median combine. The spectra were extracted using a $2''.7$ aperture centered on the target.

We also observed standard stars in order to perform relative flux calibration on the data and correct for the sensitivity of the SALT CCD. Unfortunately, due to the fixed nature of the primary mirror at the SALT telescope and the strong variation in effective aperture with time and source position, it is not possible to perform absolute flux calibration using the SALT data alone. We will report emission line flux ratios for a subsample of the objects in Section 4. We report the details of the spectroscopic observations, including observation date and total exposure time, in Table 2.

3. OPTICAL SPECTRA AND REDSHIFT DISTRIBUTION

With the assembled, final, reduced spectra, our first task was estimating the spectroscopic redshift of each object, and initial identification of emission lines was done by eye for each object. The strongest optical lines we used to constrain the redshift were Mg II $\lambda 2798$, [Ne V] $\lambda 3427$, [O II] $\lambda \lambda 3726, 3729$, [Ne III] $\lambda 3869$,

H β , and [O III] $\lambda \lambda 4959, 5007$. Additionally, the two highest-redshift objects in our sample were identified using strong UV emission lines. For the majority of the objects (29/40), we were able to identify two or more emission lines in the spectrum which we used to constrain the redshift, while for J1255–0010 there was only one strong emission line which we identified as [O II] $\lambda \lambda 3726, 3729$. Due to a strong observed 4000 \AA break to the red of the emission line in the spectrum for this object, we consider the redshift estimate for J1255–0010 to be confident. For five other objects that have a single emission line, we used the fact that there were no other strong emission lines in the spectrum to infer that the single line was most likely Mg II $\lambda 2798$, which was also observed to be broad in one of the objects (see Section 6.2 for a discussion of this object). For the remaining objects (5/40), there were no features in the spectrum allowing for accurate redshift identification. One of these objects, J1417+0108, does have a FIRST radio detection, however. In light of this, while we calculated the statistical properties of the sample using all of the estimated redshifts, we will also present statistics calculated without the five objects with a single emission feature.

Redshifts were estimated from the centroids measured using the IRAF task *splot* to fit Gaussian curves to the emission lines in each spectrum. In order to characterize the systematic error on our redshift estimates introduced due to wavelength calibration we compared SALT RSS spectra observed in a different campaign (as described in Hainline et al. 2013) to the measured SDSS spectra for these objects, and found that the average difference was on the order of $\sim 0.3 \text{ \AA}$. We can also compare the emission line measurements for the two objects in our sample for which SDSS DR9 spectra were taken: J0325–0032 ($z = 0.353$) and J0924+0027 ($z = 0.660$). For J0325–0032, the best-fit centroids for the strongest lines [O II] $\lambda \lambda 3726, 3729$ and [Ne III] $\lambda 3869$ agree to within $\sim 3 \text{ \AA}$, while for J0924+0027 the best-fit centroids for the more broad, low S/N emission line [Ne V] $\lambda 3427$ agrees to within $\sim 8 \text{ \AA}$.

In Group 1, we identified the redshift of 19/21 (90%) of the objects, and in Group 2, we identified the redshift of 16/19 (84%) of the objects (12/19, 63%, were identified with more than one emission line). For those spectra where we were able to estimate the redshift we present the rest-frame spectra in Figures 2 (Group 1) and 3 (Group 2). In these figures, we note those spectra with only one identified emission line with an asterisk. In Figure 4, we highlight our two highest-redshift sources, J0737–0052 ($z = 2.565$) and J1326–0037 ($z = 2.233$), both of which are Group 2 objects. Finally, we plot the 5 spectra in the observed frame without reliable redshift information in Figure 5. We list the spectroscopic redshifts for the sample in Table 2.

One of the fundamental properties of our *WISE*-selected sources is their redshift distribution, which we plot for our sample in the top panel of Figure 6. We plot the redshift distribution for all of the objects (excluding the two highest-redshift objects) in black, the AGNs from Group 1 in red, and the AGNs from Group 2 in blue. The full redshift distribution has an average of $\langle z_{\text{all}} \rangle = 0.52$, Group 1 has an average of $\langle z_1 \rangle = 0.35$, and Group 2 has an average of $\langle z_2 \rangle = 0.73$ (the average redshift becomes $\langle z_2 \rangle = 0.49$ without including the two $z > 2$ objects). We performed a Kolmogorov–Smirnov (K-S) two-sample test on the redshift distributions from the two groups and calculated the K-S statistic $P = 0.01$, indicating that these two samples were drawn from different distributions. We also performed the test without the five objects from Group 2 with only one

⁸ IRAF is distributed by the National Optical Astronomy Observatory, which is operated by the Association of Universities for Research in Astronomy (AURA), Inc., under cooperative agreement with the National Science Foundation.

Table 2
Sample Spectroscopic Properties

SDSS Name	Group	Obs. Date	Exp. Time (s)	z_{spec}	z_{phot}^a	[Ne III]/[O II] ^b	$^{0.0}(g - z)^c$	$\log(L_{8\mu\text{m}}/\text{erg s}^{-1})^d$
J032533.31-003216.4	1	2012 Nov	2610.6	0.353	0.140	0.44 ± 0.02	0.77 ± 0.07	44.79
J033820.71-004935.6	2	2013 Oct	2250.6	0.420	0.280	0.42 ± 0.07	0.95 ± 0.16	44.61
J035726.82-002724.9	2	2013 Oct	2250.6	0.591	0.580	44.90
J073745.20-005229.8 ^e	2	2013 Nov	1950.6	2.565	2.420	46.58
J085259.35+013715.1	1	2013 Mar	2250.6	0.268	0.160	0.23 ± 0.00	1.13 ± 0.04	44.17
J092435.55+002716.4	1	2013 Feb	2820.6	0.660	0.700	45.66
J095718.06-012049.1	2	2014 Mar	2620.6	0.711	0.660	45.33
J100346.93-011015.9	1	2013 Mar	2250.6	...	0.340	44.71 ^f
J100711.52+014627.1	1	2013 Mar	2250.6	0.170	0.220	0.11 ± 0.02	1.36 ± 0.07	44.01
J110722.11+013336.8	1	2013 Apr	2250.6	0.398	0.390	0.31 ± 0.03	1.60 ± 0.16	44.77
J112931.47+010254.7	1	2013 Mar	2250.6	0.241	0.310	0.45 ± 0.09	1.31 ± 0.10	44.49
J113635.48+015252.9	1	2013 Mar	2250.6	0.441	0.470	<0.89	2.17 ± 0.17	45.05
J115158.63-004641.2	1	2013 Mar	2250.6	0.142	0.050	0.83 ± 0.05	1.14 ± 0.02	43.60
J125521.24-001018.2	1	2013 Mar	2550.6	0.379	0.270	<5.26	1.31 ± 0.12	44.61
J130500.31+005422.1	1	2013 Mar	2250.6	0.376	0.310	0.08 ± 0.01	1.28 ± 0.10	44.74
J130845.53+015542.0	1	2013 Mar	2250.6	0.257	0.020	0.88 ± 0.10	1.23 ± 0.10	44.65
J132031.04-010248.3	2	2013 May	2250.6	0.183	0.380	<1.02	1.28 ± 0.07	43.96
J132648.81-003757.6	2	2013 May	2250.6	2.233	2.550	46.80
J133331.15-012653.3	1	2013 Feb	3000.6	0.476	0.220	0.73 ± 0.03	0.75 ± 0.15	44.96
J135423.71-000314.5	1	2013 Mar	2250.6	0.377	0.340	0.10 ± 0.01	0.96 ± 0.22	44.51
J135534.66-002206.1	2	2013 May	2250.6	0.343	0.260	44.74
J140618.16-004923.1	2	2013 May	2250.6	0.412	0.340	0.44 ± 0.06	1.13 ± 0.09	44.85
J140830.13-005001.6	2	2013 Jun	2250.6	...	0.640	45.32 ^f
J141724.04+010843.1	1	2013 Mar	2250.6	...	0.060	42.70 ^f
J143459.27-014432.8	1	2013 Mar	2250.6	0.218	0.220	0.64 ± 0.18	1.04 ± 0.10	44.10
J144006.46-011624.7	1	2013 Mar	2250.6	0.329	0.170	44.83
J144625.94-015721.9	2	2013 May	2430.6	0.441	0.700	44.81
J150539.97+013433.9	1	2013 Mar	2250.6	0.249	0.240	0.48 ± 0.07	1.25 ± 0.05	44.30
J152736.35-001007.7	2	2013 May	2250.6	0.787	0.970	44.87
J153846.30+012951.9	1	2013 Apr	2250.6	0.434	0.140	0.47 ± 0.02	0.98 ± 0.19	45.04
J154503.94-010010.4	1	2013 Mar	2250.6	0.434	0.440	0.41 ± 0.03	1.28 ± 0.13	45.22
J155421.94+001115.0	1	2013 Apr	2250.6	0.428	0.480	0.40 ± 0.07	1.67 ± 0.17	44.86
J160903.75-000426.2	2	2013 Aug	1950.6	0.264	0.210	<0.39	1.41 ± 0.27	44.17
J160928.56-013344.1	2	2014 Mar	2100.6	0.533	0.460	45.06
J163445.76-010808.6 ^e	2	2013 Aug	2250.6	0.543	0.120	44.78
J172446.04-003833.4	2	2013 Aug	2250.6	...	0.900	45.96 ^f
J173114.67-003708.1	2	2013 Aug	2250.6	0.347	0.440	43.77
J180853.93-001650.6	2	2013 Jul	2250.6	...	0.410	44.76 ^f
J194745.03-003603.8	2	2013 Aug	1950.6	0.730	0.360	45.17
J202952.16-010805.3	2	2013 Sep	2250.6	0.498	0.440	44.83

Notes.^a These photometric redshift values were estimated using SED modeling as described in Section 5.^b Flux ratio between [Ne III] $\lambda 3869$ and [O II] $\lambda\lambda 3726+3729$ emission features.^c Rest-frame $g - z$ color.^d Luminosity at $8\mu\text{m}$ estimated from the *WISE* photometry.^e These objects have broad emission lines in their observed spectra, and we classify them as Type I quasars.^f These values for $L_{8\mu\text{m}}$ were derived using z_{phot} .

emission feature, and calculated $P = 0.16$, however. While this is highly dependent on the objects in our sample where we only identify one emission feature, our results indicate that by targeting objects with fainter *W4* magnitudes, the distribution shifts to higher redshifts. This result is not surprising given the significantly shallower depth of *WISE* observations in the *W4* band as compared to the other three photometric bands. By choosing only those objects that are brightest in *W4*, we preferentially select objects at lower redshift.

We can interpret our redshift distribution in light of the results on *WISE* AGN selection described in the literature. Assef et al. (2013) describe the spectroscopic redshift distribution for a sample of *WISE*-selected AGNs ($W1 - W2 \geq 0.8$)

in the Boötes field, and demonstrate that the distribution is double-peaked for those objects in their sample with $W2 < 15.73$. The main peak is between $1 < z < 2$, while there is a smaller peak at $z \sim 0.25-0.5$. The authors propose that the *WISE* sensitivity results in recovering obscured AGNs at lower redshifts, where emission from these objects dominate the *W1* and *W2* photometric bands. As the redshift increases, the *W1*–*W2* color criteria is less efficient at selecting obscured quasars since the portion of the SED probed by the *W1* and *W2* photometric bands moves to shorter wavelengths where the obscured AGN emission is not as dominant compared to host galaxy emission. This effect leads to a minimum in the distribution at $z \sim 0.75$, although there is an increase beyond

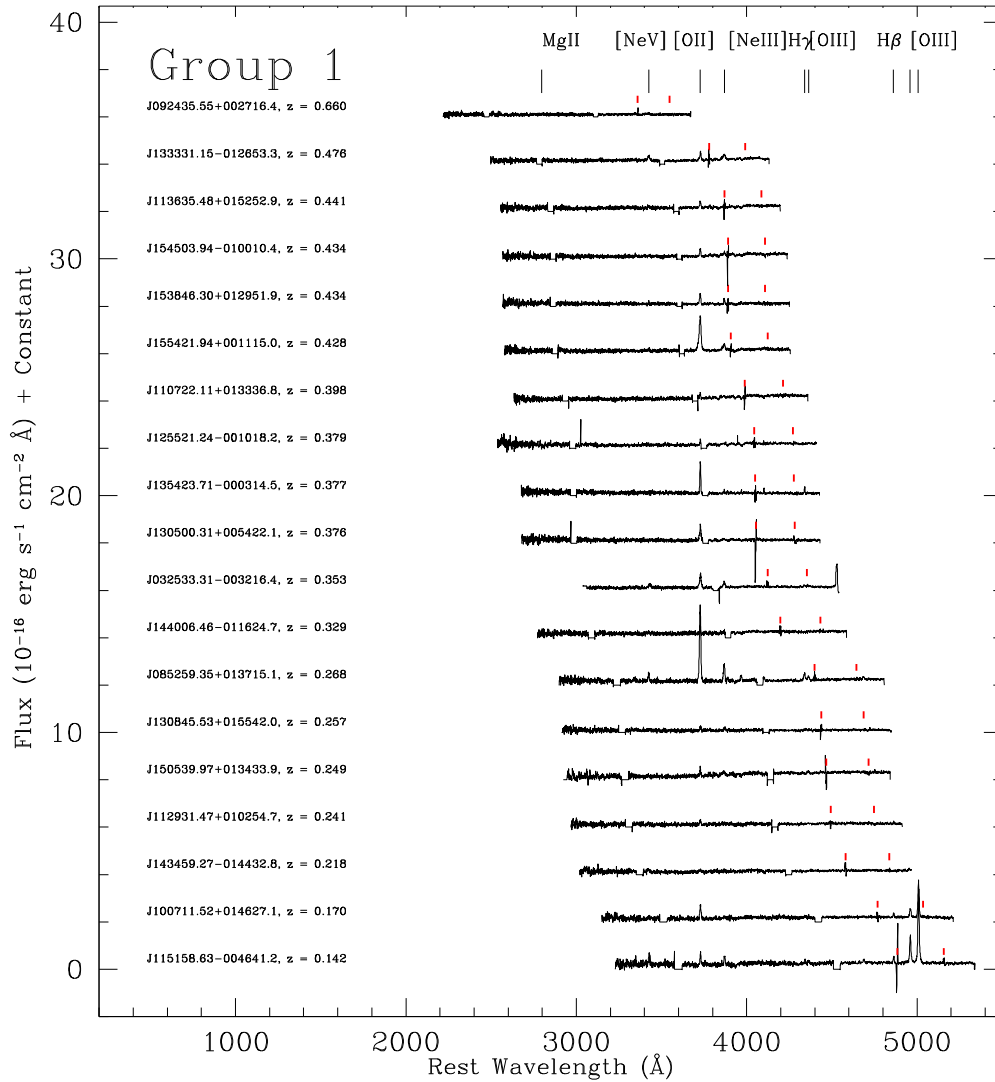


Figure 2. Rest-frame spectra for objects in Group 1. We plot only those objects with redshift determinations that could be made from identifying one or more emission lines in the observed frame spectrum. We also plot the positions of the strongest optical lines used for determining redshift above the spectra, and indicate the two strongest sky features in each spectrum with red vertical lines.

(A color version of this figure is available in the online journal.)

that due to a larger comoving volume being observed. The distribution of redshifts for our SALT targets is very similar to the peak at $z \sim 0.25\text{--}0.5$ from the Assef et al. (2013) distribution. The vast majority of our objects have $z < 0.75$, and the two bright $z \sim 2$ AGNs also agree with the higher- z tail of the Assef et al. sample.

As we probed objects with fainter $W4$ magnitudes, between Groups 1 and 2, we found that our distribution moved to higher redshifts, but the lack of objects at $1 < z < 2$ in our sample is most likely a result of our initial optical selection criteria of $20 < g < 22$. For obscured quasars, the g -band probes host galaxy emission, and so this cut limits our galaxy selection to lower redshifts. To test this assumption, we explored a large catalogue of ~ 4000 galaxies with photometric redshifts and SDSS identifications from the Boötes field. For all objects with $20 < g < 22$, the average (median) photometric redshift is only $0.43(0.37) \pm 0.24$, demonstrating the impact a SDSS g -band magnitude cut can have at selecting high-redshift galaxies.

These redshifts, along with the *WISE* photometry in the $W2$, $W3$, and $W4$ bands, can be used to estimate an AGN IR luminosity. Following the analysis presented in Hainline et al.

(2013), we used the *WISE* photometry to estimate a luminosity at rest-frame $8\text{ }\mu\text{m}$ ($L_{8\text{ }\mu\text{m}}$). For this estimate, we modeled the AGN mid-IR emission with a power law and do not account for the individual filter response functions, although, based on the *WISE* colors for these objects, any flux corrections would be on the order of a few percent (Wright et al. 2010). We also assume that the flux is measured at the central wavelength for each filter. In Section 5, we describe the use of galaxy and AGN templates to model the broadband SEDs for these objects, and we can also use the best-fit AGN template to estimate the $8\text{ }\mu\text{m}$ AGN luminosity for each object in our sample. We find that luminosities measured from the best-fit templates agree with those estimated from the *WISE* photometry (and presented in Table 2) to within 0.2 dex. Excluding the two high-redshift sources, the objects in our sample have a range in $8\text{ }\mu\text{m}$ luminosity of $\log(L_{8\text{ }\mu\text{m}}) = 44.0\text{--}45.0$, with an average (median) of $\langle \log(L_{8\text{ }\mu\text{m}}) \rangle = 44.9(44.8)$. In order to compare the luminosities to those from quasars in the literature, we plot the $8\text{ }\mu\text{m}$ luminosity against the redshift for our sample in Figure 6. For comparison, we also plot the estimated $8\text{ }\mu\text{m}$ luminosities from the SDSS Type II quasar sample (with $W1$, $W2$, $W3$,

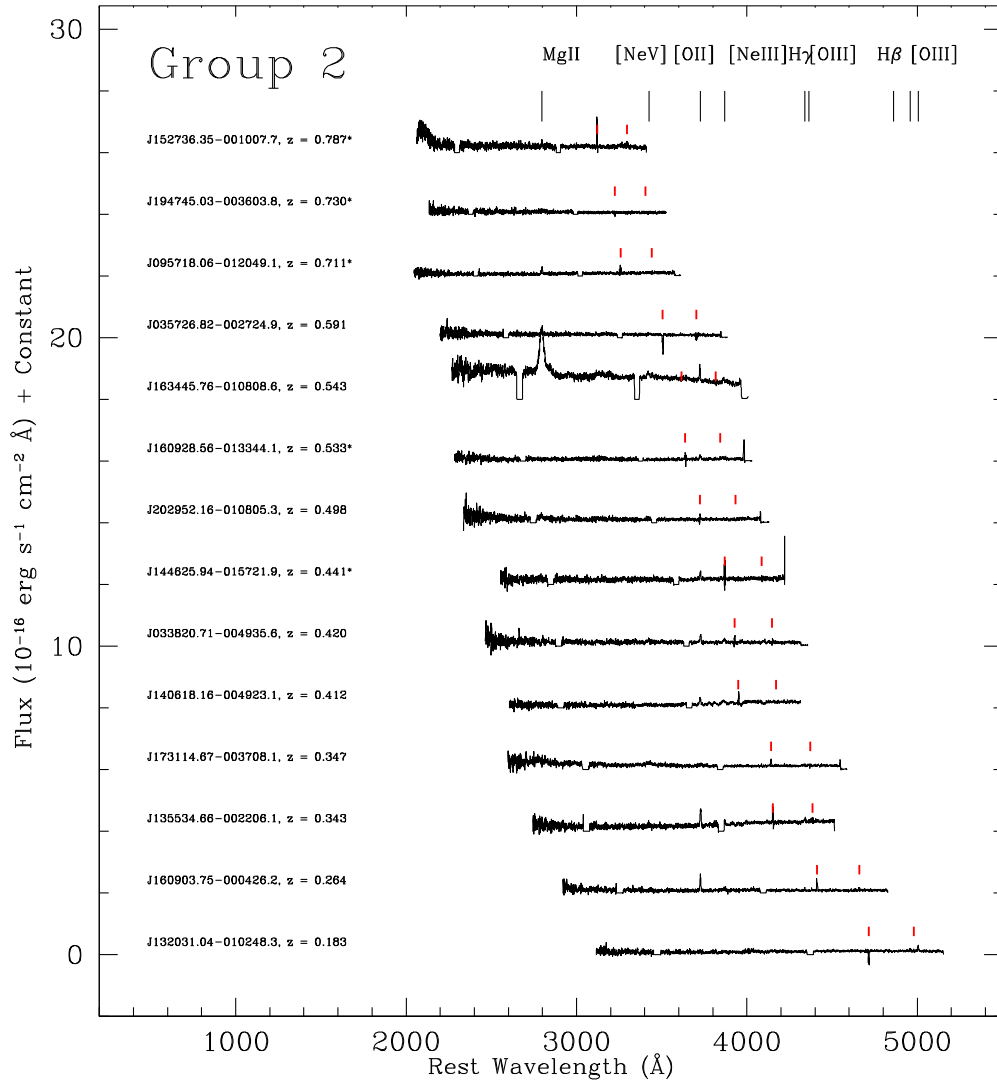


Figure 3. Same as Figure 2, but for those objects from Group 2. We also indicate with an asterisk which objects have redshift determinations from a single emission line.

(A color version of this figure is available in the online journal.)

$S/N > 3.0$) from Reyes et al. (2008) ($\langle z \rangle = 0.324$, $z_{\text{median}} = 0.279$), with an average (median) of $\langle \log(L_{8\mu\text{m}}) \rangle = 44.7(44.3)$, as well as the estimated $8\mu\text{m}$ luminosities for the SDSS Type I quasar sample (with $W1$, $W2$, $W3$, $S/N > 3.0$) from Shen et al. (2011; for the quasars at $z < 0.84$, $\langle z \rangle = 0.519$, $z_{\text{median}} = 0.529$), with an average (median) of $\langle \log(L_{8\mu\text{m}}) \rangle = 45.0(44.8)$ (we restrict the objects used in this average to those with $z < 0.84$, the upper limit on the redshifts from the Reyes et al. 2008 sample). Based on these results, if the mid-IR is dominated by AGN emission for the objects in our sample, these AGNs would lie in the quasar regime. Notice, however, that at each redshift, the objects that comprise our sample are at systematically higher IR luminosities compared to the optically selected sample, as would be expected from *WISE* selection.

4. EMISSION LINE DIAGNOSTICS

The objects that comprise our sample were selected from their IR colors to be AGNs. To test the success of our selection criteria, we sought to examine whether excitation of the narrow emission lines in our objects was driven by AGN activity or SF. We can compare the strong optical emission lines present in our

spectra in order to explore the source of the excitation. We fit emission lines in our observed spectra with a single Gaussian. For the narrow emission lines, we forced the width of each fitted line to be the same. To estimate uncertainties on the line fluxes, we used a Monte Carlo approach. For each object we generated 500 artificial spectra by perturbing the flux at each wavelength of the true spectrum by a random amount consistent with the 1σ error spectrum. For each artificial spectrum, we measured the line fluxes using the same procedure as was done on the true spectrum. The standard deviation of the distribution of line fluxes measured from the artificial spectrum was used as the error on the true line flux measurement. For each object, if a line was detected with less than 3σ significance we used a measure of 3σ as the maximum flux for the line, and report an upper limit.

For nearby galaxies the optical emission-line ratios of $[\text{OIII}] \lambda 5007/\text{H}\beta$ as well as $[\text{NII}] \lambda 6584/\text{H}\alpha$ are commonly compared to separate Type II AGNs from star-forming galaxies (the Baldwin, Phillips & Terlevich, or “BPT diagram”; Baldwin et al. 1981). Collisionally excited emission lines $[\text{OIII}] \lambda 5007$ and $[\text{NII}] \lambda 6584$ are much stronger in AGNs, which produce a much harder ionizing spectrum, relative to the recombination lines $\text{H}\alpha$ or $\text{H}\beta$. In the BPT

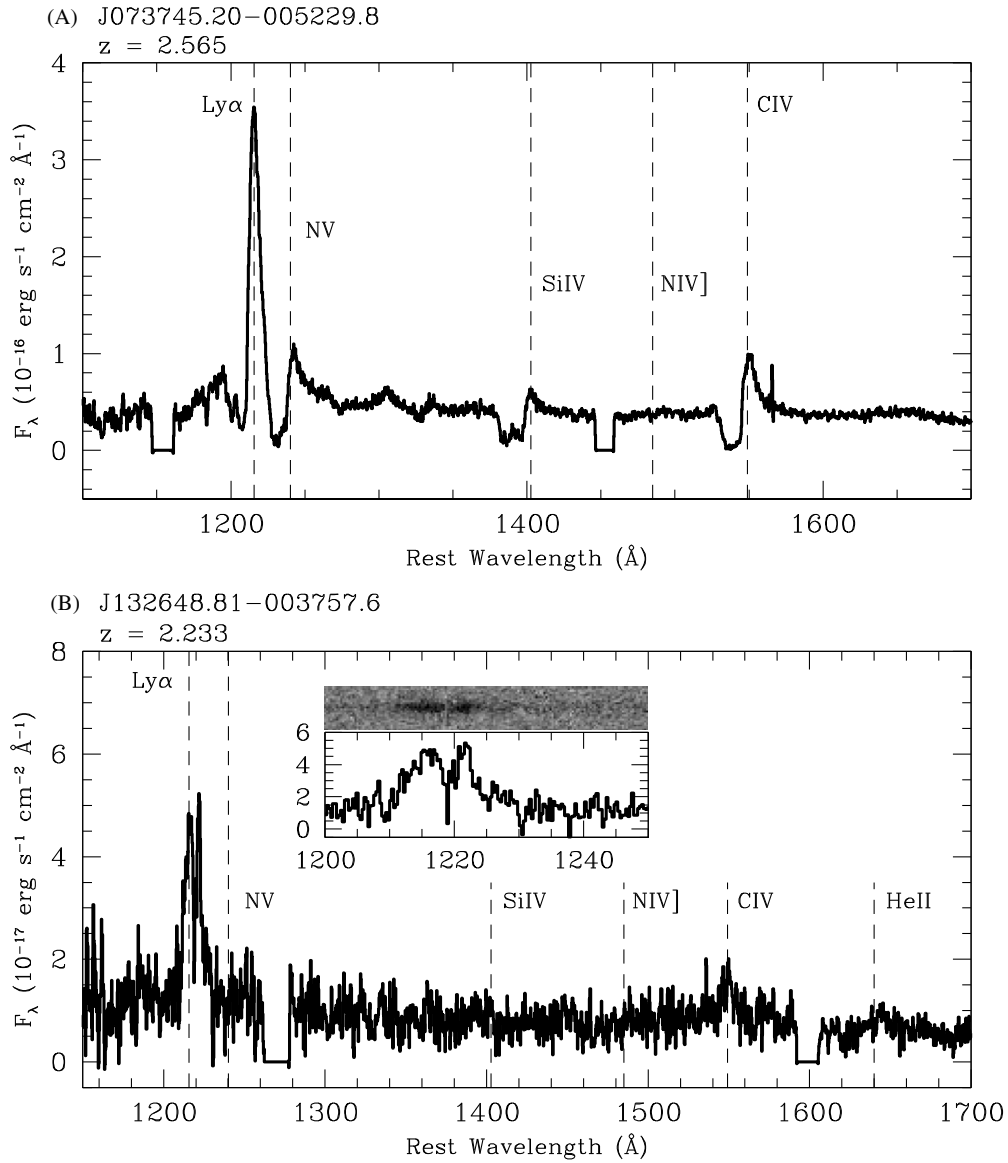


Figure 4. Rest-frame spectra for the two high-redshift objects J0737–0052 (A, $z = 2.565$) and J1326–0037 (B, $z = 2.233$), both from Group 2. For J0737–0052, the presence of Ly α , NV $\lambda 1240$, and CIV $\lambda 1548$ in emission is indicative of the presence of an AGN in this object. The broad absorption features seen to the blue of each strong emission line indicates that this object is most likely a broad absorption line quasar. The spectrum for J1326–0037 shows Ly α and CIV $\lambda 1548$ in emission, and in the inset, we plot a zoom on the Ly α line as well as the two-dimensional spectrum.

diagram, the position of an object falls into one of three commonly defined areas based on the emission-line ratios of [O III] $\lambda 5007/\text{H}\beta$ as well as [N II] $\lambda 6584/\text{H}\alpha$: an AGN region, a star-forming locus, and a region where “composite” objects with evidence for both AGN activity and SF are found. The usage of these emission lines is limited, however, to redshifts where the emission lines are still present in the wavelength range covered by the spectrograph. The SALT RSS set-up that was used for this study spans an observed wavelength range to 6100 \AA , which excludes [N II] $\lambda 6584$ and $\text{H}\alpha$, and we can only observe [O III] $\lambda 5007$ to $z < 0.22$.

There are three objects in our assembled sample (J1151–0046, J1007+0146, J1320–0102) with $z < 0.22$, and for these objects, we observe [O III] $\lambda 5007$ and $\text{H}\beta$ with high S/N. For these sources, $\log([\text{O III}] \lambda 5007/\text{H}\beta) \geq 0.9$, a ratio which is strongly indicative of AGN activity. For the two objects with SDSS spectra, we calculated the [O III]/ $\text{H}\beta$ ratio as well. For J0325–0032, $\log([\text{O III}] \lambda 5007/\text{H}\beta) = 1.1$ and

$\log([\text{N II}] \lambda 6584/\text{H}\alpha) = -0.11$, which puts this object firmly in the AGN regime on the BPT diagram (Kauffmann et al. 2003; Kewley et al. 2006). For J0924+0027, $\log([\text{O III}] \lambda 5007/\text{H}\beta) = 0.7$, and as $z = 0.660$, the SDSS spectrum does not cover [N II] or $\text{H}\alpha$. Additionally, we can use the [O III] luminosity for those objects in our sample with [O III] detections to confirm the results for the luminosity regime spanned by our sample. While the fixed primary mirror of SALT prevents us from measuring the luminosity for the [O III] lines in the spectra where the line appears (due to our inability to perform absolute flux calibration), we measured the [O III] luminosity for the two objects with SDSS spectra. For J0924+0027, we measure $\log(L_{[\text{O III}]}/\text{erg s}^{-1}) = 42.79$, while for J0325–0032, we measure $\log(L_{[\text{O III}]}/\text{erg s}^{-1}) = 42.63$. Both of these values are well above the limit of $\log(L_{[\text{O III}]}/\text{erg s}^{-1}) > 41.88$ used by Reyes et al. (2008) to select Type II quasars from SDSS.

For objects with $z > 0.22$, we cannot use [O III] $\lambda 5007/\text{H}\beta$ to test the ionization source. Instead, we used

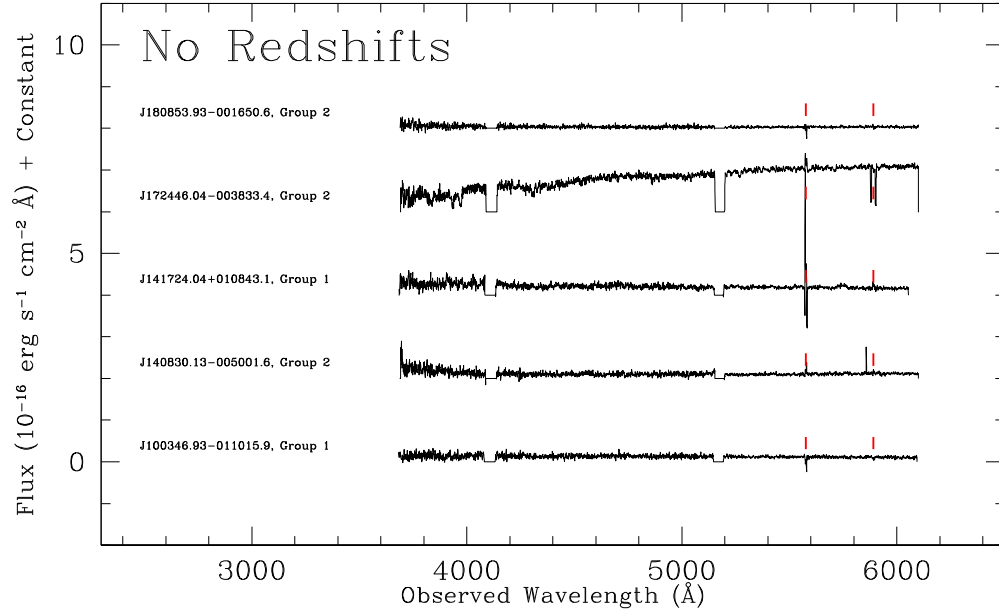


Figure 5. Observed-frame spectra for the objects in our sample without reliable redshift estimates. We indicate the group that each object belongs to on the figure. (A color version of this figure is available in the online journal.)

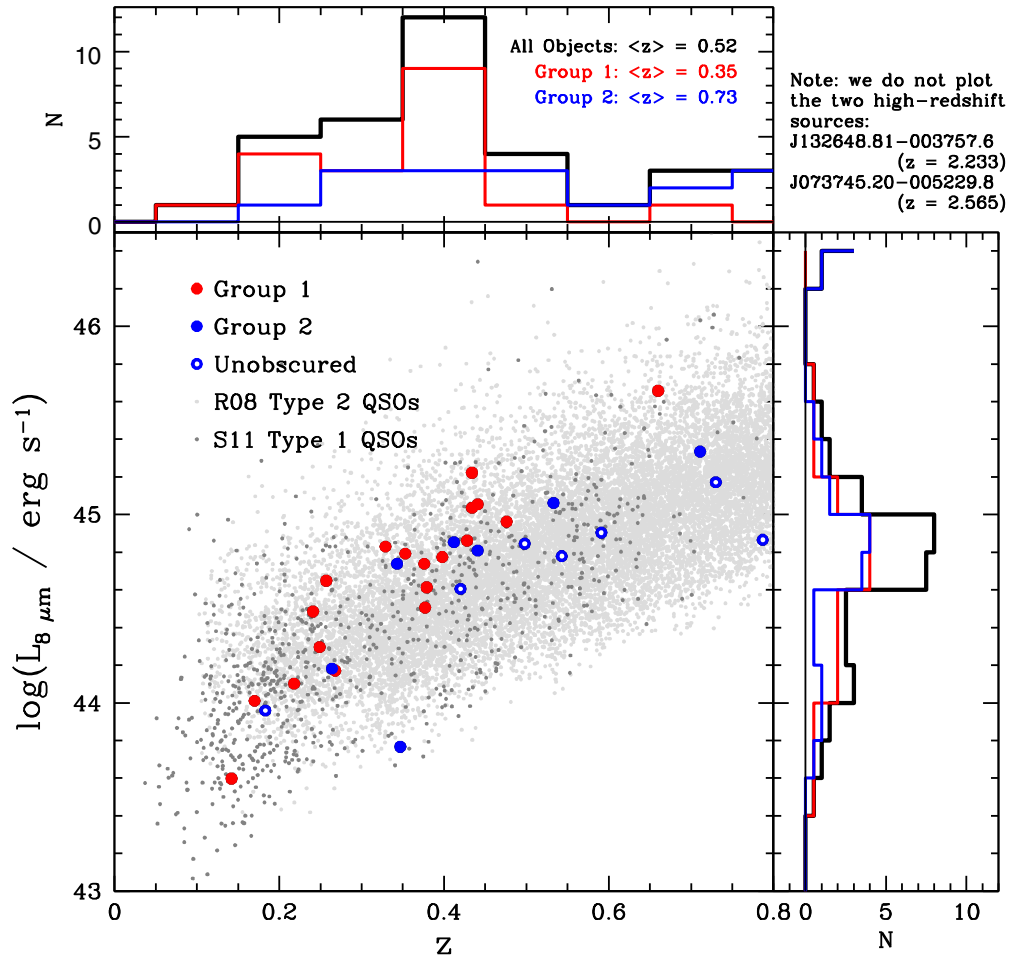


Figure 6. *WISE* 8 μm luminosity plotted against spectroscopic redshift for the objects in our sample. We also show the IR luminosities and redshifts for the SDSS Type I quasar sample from Shen et al. (2011) in light gray, and the SDSS Type II quasar sample from Reyes et al. (2008) in dark gray. For both of these comparison samples, we only plot 8-micron luminosities for objects with *WISE* W1, W2, and W3 S/N > 3.0. Our SALT sample is plotted with red (Group 1) and blue (Group 2) points (with unobscured objects from the SED fitting shown with open circles), and we also show histograms of the distributions on the top and right sides of the figure. We truncate the plot at $z \sim 0.8$ and do not show the two highest-redshift objects in our sample. The objects in our SALT sample have IR luminosities that span the full range observed for both Type I and II quasars, although, at a given redshift, our selection criteria does preferentially choose the most IR-luminous objects as compared to those selected optically.

(A color version of this figure is available in the online journal.)

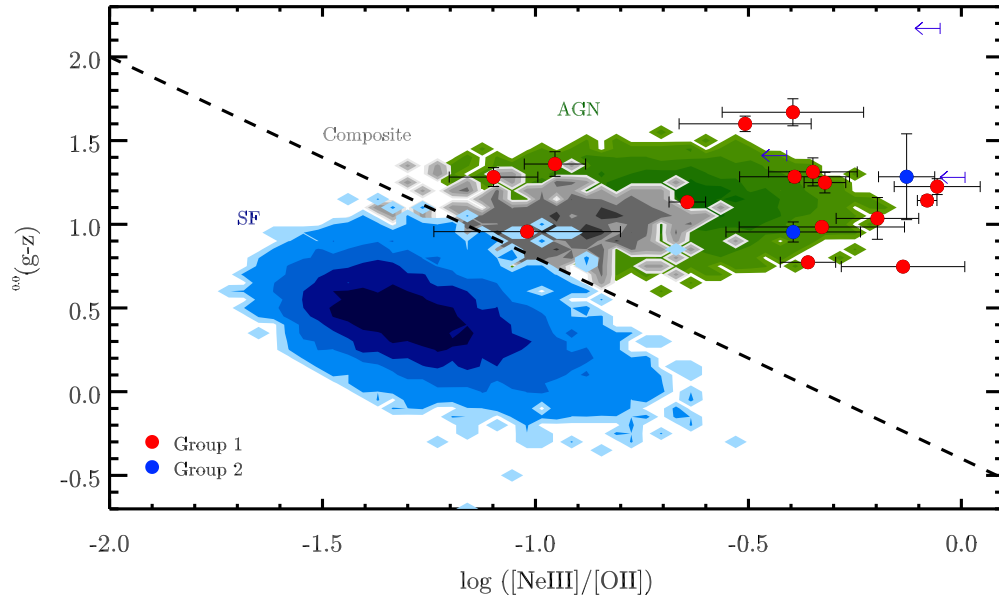


Figure 7. Rest-frame $g - z$ color plotted against $\log([\text{Ne III } \lambda 3869]/[\text{O II } \lambda \lambda 3726+3729])$ (“TBT diagram”; Trouille et al. 2011). The objects in our sample with significant $[\text{Ne III } \lambda 3869]$ and $[\text{O II } \lambda \lambda 3726+3729]$ emission line flux measurements are plotted with red (Group 1) and blue (Group 2) circles. We also plot SDSS galaxies from Trouille et al. (2011); those with BPT and TBT emission lines detected with $\text{S/N} > 5$ with colored contours. In green, we plot contours for the SDSS BPT AGNs, in blue we plot the SDSS BPT star-forming galaxies, and in gray we plot the BPT composite objects. We show the empirical separation between AGNs and star-forming galaxies used in Trouille et al. (2011). The SALT objects with measured TBT emission lines occupy the region dominated by AGNs.

(A color version of this figure is available in the online journal.)

a different emission line diagnostic, $[\text{Ne III } \lambda 3869]/[\text{O II } \lambda \lambda 3726+3729]$. This line ratio is used in the Trouille, Barger & Tremonti diagram (“TBT diagram”; Trouille et al. 2011), a plot that compares $[\text{Ne III } \lambda 3869]/[\text{O II } \lambda \lambda 3726+3729]$ to the rest-frame $g - z$ color (which we will refer to as $^{0.0}(g - z)$) for galaxies at intermediate redshifts, and can be used to separate AGNs and star-forming galaxies with a high degree of confidence. While $[\text{Ne III } \lambda 3869]$ is weaker than the strong $[\text{O III } \lambda 5007]$ emission line, it is also indicative of highly ionized gas excited by an AGN, and separates AGNs from metal-rich star-forming galaxies. The rest-frame $g - z$ color helps to separate AGNs from metal-poor star-forming galaxies, as they tend to be dominated by their bulge components, and are significantly redder. Trouille et al. (2011) demonstrate the success of the TBT diagram in recovering both SDSS BPT-selected AGNs (98.7% of the objects in their sample) as well as BPT-selected star-forming galaxies (97%).

Our usage of the TBT diagram is limited to $z < 0.59$ where $[\text{Ne III } \lambda 3869]$ appears on the RSS chip in our observational set-up. We measured the line flux ratios between the $[\text{Ne III } \lambda 3869]$ and $[\text{O II } \lambda \lambda 3726+3729]$ emission features, where we fit both lines simultaneously. For six objects, either $[\text{Ne III } \lambda 3869]$ or $[\text{O II } \lambda \lambda 3726+3729]$ fell on a gap between the detector chips or on a bright sky feature, and as a result, we cannot report a line flux ratio. For J0325–0032, we can also compare the line flux ratio measured from our SALT spectrum against the ratio measured from the SDSS spectrum. For this object, we calculate $\log([\text{Ne III } \lambda 3869]/[\text{O II } \lambda \lambda 3726+3729]) = -0.36 \pm 0.02$ from the SALT spectrum, and $\log([\text{Ne III } \lambda 3869]/[\text{O II } \lambda \lambda 3726+3729]) = -0.39 \pm 0.02$ from the SDSS spectrum, consistent within the given uncertainties.

To determine $^{0.0}(g - z)$ we start with the SDSS *ugriz* photometry and follow the methodology from Trouille et al. (2011), using *kcorrect* v4.2 (Blanton & Roweis 2007) to estimate the rest-frame g and z magnitudes. Uncertainties on the rest-frame colors are estimated by creating 500 artificial sets of photometry for each object, where each artificial magnitude was

created by randomly altering the observed SDSS photometry by an amount consistent with the uncertainties. We then ran the *kcorrect* software on each set of artificial magnitudes, and report the standard deviation on the distribution of resulting $^{0.0}(g - z)$ values as the uncertainty in the true value. We report both the $[\text{Ne III } \lambda 3869]/[\text{O II } \lambda \lambda 3726+3729]$ line ratios as well as the $^{0.0}(g - z)$ values for each of the objects in our sample in Table 2.

We plot those targets with $[\text{Ne III } \lambda 3869]/[\text{O II } \lambda \lambda 3726+3729]$ ratios on the TBT diagram in Figure 7. This figure also includes contours for a large sample of SDSS emission-line galaxies at $0.02 < z < 0.35$ from Trouille et al. (2011), with emission-line fluxes measured by MPA-JHU (Aihara et al. 2011). Contours for BPT-selected AGNs are shown in blue, BPT star-forming galaxies are shown in green, and BPT composite objects are shown in gray. The objects in our sample are plotted with red and blue circles depending on their selection group, and we plot those objects with upper limits on the flux ratio with an arrow.⁹ Our sources are mostly found clustered to the top of the figure, located in the region of the diagram dominated by BPT AGNs, and are distinctly separate from star-forming galaxies.

For those objects for which we can use emission lines (either optical or UV) to estimate the source of the ionizing radiation, there is strong evidence that the *WISE* selection criteria is targeting AGNs. However, there does exist a sample of objects without optical evidence for AGN activity. There are four objects with upper limits on the ratio of $[\text{Ne III } \lambda 3869]/[\text{O II } \lambda \lambda 3726+3729]$: J1136+0152, J1255–0010, J1320–0102, and J1609–0004. As discussed above, J1320–0102 is at a low redshift and we measure the flux ratio of $\log([\text{O III } \lambda 5007]/\text{H}\beta) = 0.9$, which is indicative of an AGN. For the other three objects, if they are indeed star-forming galaxies rather than AGNs, this implies a contamination fraction in our sample of 3/23 ($\sim 13\%$) (We only compare these three objects to those galaxies where we can measure the $[\text{O III } \lambda 5007]/\text{H}\beta$,

⁹ In order to focus on the bulk of the population, one object with an upper limit of $[\text{Ne III } \lambda 3869]/[\text{O II } \lambda \lambda 3726+3729] < 5.26$, J1255–0010, does not appear on the plot.

[Ne III]/[O II], or UV emission lines). This contamination fraction agrees with the fraction of non-active galaxies observed in the *Spitzer*-selected AGN sample presented in Lacy et al. (2013; 22%). If we include the five objects in our sample without spectroscopic redshifts, assuming that they are star-forming galaxies, the contamination fraction would have an upper limit of $\sim 30\%$ (8/28). In the next section, we discuss the use of SED modeling to further explore the AGN activity in our sample.

5. SED MODELING

Existing optical through infrared photometry for the objects comprising our sample allows us to explore their SEDs. SED decomposition is a powerful tool for gaining physical insight into the AGN and host galaxy properties of our sample, and it can also be used to estimate the redshift for those objects where we do not observe emission features in the spectrum. In order to best model the SEDs, we supplement the SDSS and *WISE* photometry described in Section 2 with near-IR Y , J , H , and K photometry from the UKIRT Infrared Deep Sky Survey (UKIDSS; Lawrence et al. 2007) Large Area Survey. We use the extended source aperture-corrected magnitudes with a $5''.7$ aperture measured with $>3\sigma$ significance. We have UKIDSS data for 23 objects. For an additional three objects where UKIDSS data was not available, we also used near-IR J , H , and K photometry from the Two Micron All-Sky Survey (2MASS; Skrutskie et al. 2006) Point Source Catalogue where an object was detected in an individual filter with $>3\sigma$ significance. As this SED modeling is only designed to explore the relationship between the host galaxy and quasar emission for each object in our sample, we use the catalogue uncertainties for estimating the best fits but, as we are not accounting for all of the observational errors, we follow Chung et al. (2014) and assign a conservative minimum photometric error of 0.05 mag on each measurement, which is comparable to or smaller than the photometric calibration uncertainties for each survey (Hewett et al. 2006; Skrutskie et al. 2006; Ahn et al. 2012; Cutri et al. 2013).

For the fitting, we follow the methodology we model each galaxy as a linear combination of a single galaxy template and a reddened AGN template (note that this is different from the methodology discussed in Assef et al. 2010, where each galaxy was modeled as a linear combination of all three galaxy templates plus an AGN template). We use the empirically-derived models from Assef et al. (2010), which consist of three galaxy templates (a spiral “Sbc,” elliptical “E,” and irregular “Im” galaxy), as well as an unobscured AGN template. In order to simulate the effects of AGN obscuration, we follow Assef et al. (2010) and apply an extinction model to the AGN template that consists of a Small Magellanic Cloud (SMC) like extinction curve at $\lambda < 3300 \text{ \AA}$ (Gordon & Clayton 1998) and a Galactic extinction curve at longer wavelengths (Cardelli et al. 1989), with $R_V = 3.1$ for both, and in this paper we parameterize the extinction using $E(B - V)$. Because we are attempting to fit an unobscured AGN template to objects with varying amounts of dust obscuration, we follow Mainieri et al. (2011) and Hainline et al. (2012) and employ an additional prior of $E(B - V)_{\text{AGN}} > 1.0$ for those objects with evidence indicating that they are an obscured AGN. We use this prior on objects with an SDSS TYPE flag of “3,” indicating that the galaxy is resolved in optical imaging. For these objects, we assume that the optical portion of the SED is dominated by stellar emission rather than that of the central AGN. Setting a lower bound on the best-fit

extinction value was only required for fitting six objects out of the total 35 that we modeled in this way, and the fits were not made significantly worse by using this prior. For each object, we calculated the monochromatic flux densities from the observed photometry,¹⁰ and compared these values to the flux densities from the best-fit templates passed through the SDSS, UKIDSS, 2MASS, and *WISE* bandpass filters, and used χ^2 minimization to find the best fits for each object. The output parameters are then two coefficients for the linear combination (a galaxy and an AGN coefficient), and a value for $E(B - V)_{\text{AGN}}$. The results from our fitting are shown in Table 3 and Figures 8–9.

As can be seen from the best-fit χ^2 values, the majority of the objects in our sample are well fit by the Assef et al. (2010) templates. J1355–0022 has $\chi^2_{\text{red}} > 40$, due primarily to the Assef et al. AGN template being redder than the observed W3–W4 color. We observe a large variety in the optical SED shapes for the objects in our sample, and all three galaxy templates are used in our best-fit models. For each object, the best-fit AGN coefficients are above zero, indicating that galaxy light alone is unlikely to be the source of the infrared emission seen in the SEDs. For the three objects described in the previous section that do not show evidence in their optical spectra for an AGN, we do recover non-zero AGN coefficients, but these SEDs would also perhaps be fit using a more extreme star-forming template than the one derived in Assef et al. (2010). Indeed, the SEDs of both M82 and Arp220 taken from the SWIRE template library (Polletta et al. 2007) have stronger mid-IR emission from dust heated by SF, which fits the *WISE* photometry for the objects in our sample with the highest values for $E(B - V)_{\text{AGN}}$. For each object, we also calculate $f_{\text{AGN}, 1 \mu\text{m}}$, which is defined as the fraction of the total emission in the best-fit model at rest-frame $1 \mu\text{m}$ that is contributed by the AGN template (Hainline et al. 2012). We list these values in Table 3. There are 16 objects with $f_{\text{AGN}, 1 \mu\text{m}} < 0.01$, which we note in the table. To check the validity of our SED fits, we examined the far-infrared luminosities and star-formation rates (SFRs) implied by the best-fit galaxy coefficients. The Assef et al. (2010) templates only extend to a rest-frame wavelength of $\sim 30 \mu\text{m}$, and so we used Chary & Elbaz (2001) far-infrared star-forming galaxy templates to predict the far-infrared luminosity from SF for our sample. We passed the observed best-fit galaxy template (ignoring the AGN component) through the *Spitzer* MIPS $24 \mu\text{m}$ passband, and then used this flux to constrain the Chary & Elbaz (2001) templates, which were integrated to produce the far-infrared luminosity from SF for each object. We then used the conversion from Kennicutt (1998) to calculate the SFRs. We measure an average (median) SFR for the sample (without the two high-redshift objects) of $16 (6) M_{\odot} \text{ yr}^{-1}$, in agreement with expectations for massive star-forming galaxies at the redshift range probed by our sample. We note that this method is highly uncertain, especially without longer-wavelength observations to better constrain the far-infrared templates.

In order to estimate redshifts for those objects in our sample without detected emission lines, we ran the SED analysis as described above on each of the objects in our sample but allowed redshift to be a free parameter. Estimating redshifts from AGN photometry is difficult as the power-law shape of an AGN SED with minimal extinction creates a degeneracy between color and redshift which requires long wavelength photometric coverage to break (Brodwin et al. 2006; Salvato et al. 2009,

¹⁰ For the *WISE* photometry, we used the conversions provided in Section IV.4.h.i of the *WISE* All-Sky Data Release Explanatory Supplement.

Table 3
Best-fit SED Parameters

Object	Group	Template ^a	Gal. Coeff ^a	AGN Coeff ^a	$E(B - V)_{\text{AGN}}^a$	$\chi^2_{\text{red}}^a$	$f_{\text{AGN}, 1\mu\text{m}}^b$
J032533.31–003216.4	1	Sbc	$9.21e-16$	$2.47e-16$	4.72	21.86	<0.01
J033820.71–004935.6	2	Sbc	$6.01e-16$	$6.82e-17$	0.35	2.16	0.23
J035726.82–002724.9	2	E	$2.32e-16$	$7.90e-17$	0.26	1.46	0.32
J073745.20–005229.8	2	Im	$1.05e-16$	$1.16e-16$	0.10	11.88	0.51
J085259.35+013715.1	1	Sbc	$1.12e-15$	$1.38e-16$	15.61	16.91	<0.01
J092435.55+002716.4	1	Sbc	$1.44e-15$	$4.03e-16$	1.00 ^c	15.25	0.26
J095718.06–012049.1	2	Sbc	$1.29e-15$	$1.14e-16$	3.98	8.97	<0.01
J100711.52+014627.1	1	Sbc	$1.29e-15$	$2.03e-16$	5.53	2.64	<0.01
J110722.11+013336.8	1	E	$6.42e-16$	$1.90e-16$	5.53	6.24	<0.01
J112931.47+010254.7	1	Sbc	$1.27e-15$	$2.98e-16$	5.52	9.86	<0.01
J113635.48+015252.9	1	Sbc	$1.63e-15$	$2.17e-16$	1.00 ^c	8.09	0.14
J115158.63–004641.2	1	Sbc	$9.75e-16$	$1.38e-16$	9.38	15.55	<0.01
J125521.24–001018.2	1	Sbc	$1.54e-15$	$1.16e-16$	8.69	11.35	<0.01
J130500.31+005422.1	1	Sbc	$1.84e-15$	$6.10e-16$	47.72	16.30	<0.01
J130845.53+015542.0	1	Sbc	$4.30e-16$	$3.16e-16$	1.00 ^c	9.80	0.48
J132031.04–010248.3	2	E	$2.47e-16$	$1.50e-16$	0.61	11.96	0.36
J132648.81–003757.6	2	Im	$1.14e-16$	$1.82e-16$	0.54	6.07	0.47
J133331.15–012653.3	1	Sbc	$1.78e-15$	$7.53e-16$	53.38	31.81	<0.01
J135423.71–000314.5	1	Im	$5.82e-17$	$3.24e-16$	27.50	4.18	<0.01
J135534.66–002206.1	2	E	$7.85e-16$	$2.24e-16$	1.00 ^c	43.56	0.14
J140618.16–004923.1	2	Sbc	$1.40e-15$	$1.54e-16$	1.86	13.59	0.05
J143459.27–014432.8	2	Sbc	$1.20e-15$	$2.23e-16$	14.01	10.31	<0.01
J144006.46–011624.7	1	Sbc	$1.34e-15$	$2.42e-16$	1.00 ^c	13.79	0.18
J144625.94–015721.9	2	Sbc	$8.03e-16$	$1.24e-16$	1.00 ^c	14.45	0.16
J150539.97+013433.9	1	Sbc	$1.34e-15$	$2.05e-16$	11.63	4.02	<0.01
J152736.35–001007.7	2	E	$6.11e-16$	$8.50e-17$	0.22	16.89	0.17
J153846.30+012951.9	1	Sbc	$8.47e-16$	$2.76e-16$	7.34	13.15	<0.01
J154503.94–010010.4	1	Sbc	$1.80e-15$	$3.31e-16$	1.76	11.29	0.09
J155421.94+001115.0	1	E	$9.63e-16$	$2.20e-16$	6.71	26.44	<0.01
J160903.75–000426.2	2	Sbc	$7.58e-16$	$8.31e-17$	2.36	0.96	0.03
J160928.56–013344.1	2	E	$9.26e-16$	$1.65e-16$	4.12	5.67	<0.01
J163445.76–010808.6	2	E	$1.76e-16$	$1.16e-16$	0.26	15.50	0.48
J173114.67–003708.1	2	Im	$5.04e-17$	$2.64e-17$	0.56	1.29	0.22
J194745.03–003603.8	2	E	$8.56e-17$	$7.04e-17$	0.36	2.31	0.50
J202952.16–010805.3	2	Sbc	$8.06e-16$	$9.83e-17$	0.45	6.45	0.22

Notes.

^a Parameters from the SED fits using the templates from Assef et al. (2010). Each fit was done using one galaxy template, along with the dust obscured AGN template with obscuration parameterized by $E(B - V)_{\text{AGN}}$. We also provide the reduced χ^2 value for each fit.

^b Fraction of the total emission at rest-frame $1\mu\text{m}$ that is estimated to arise from AGN emission.

^c For these objects, the fits were restricted to $E(B - V)_{\text{AGN}} \geq 1.0$ due to the objects being resolved in optical SDSS imaging, and most likely unobscured AGNs.

2011). We examined the photometric redshifts recovered for those objects with spectroscopic redshifts, as well as those with existing SDSS photometric redshifts (Oyaizu et al. 2008; photo- z 's were estimated for each object that was resolved in SDSS imaging, and these values largely agree with the spectroscopic redshifts for these objects). For our own photometric redshift calculation, we used the χ^2 values to explore the 2σ confidence intervals and find the best physical fit to the data for each object, incorporating the $E(B - V)_{\text{AGN}} > 1.0$ prior discussed above for objects that were resolved in SDSS imaging. In a few cases, we rejected best fits at large redshifts ($z > 2$) both due to the low likelihood of a galaxy with $20 < g < 22$ to be at higher redshift (see our analysis of the AGNs in this optical photometric range in the Boötes field in Section 3) and the low likelihood of a quasar to be this luminous at such high redshift, based on the observed quasar luminosity function (Hopkins et al. 2007). The final photometric redshifts estimated from this procedure are given in Table 2. In Figure 10, we plot the spectroscopic redshifts we derived from our optical spectra against the photometric redshifts we derived from this process for objects with $z < 1.0$.

Overall, there is excellent agreement between the spectroscopic and photometric redshifts for the majority of the objects in our sample, although our recovered photometric redshifts are often low in comparison to the corresponding spectroscopic redshifts. The two most discrepant objects, J1634–0108 and J1947–0036 have SEDs that are dominated by AGN emission ($f_{\text{AGN}, 1\mu\text{m}} \sim 0.5$, and $E(B - V)_{\text{AGN}} < 0.4$).

With these uncertainties in mind, we estimated the photometric redshift for the five objects in our sample without spectroscopic redshifts seen in Figure 5. We plot the best-fit SEDs in Figure 11 and report the calculated photometric redshifts for these sources in Table 2. As can be seen, these objects have a range of $0.1 < z_{\text{phot}} < 0.9$, in broad agreement with the spectroscopic redshifts observed for our sample. If these photometric redshifts are roughly correct, then we calculate an average redshift of $z = 0.52$ for all of the objects in our sample, while Group 1 has an average redshift of $z = 0.36$, and Group 2 has an average redshift of $z = 0.71$ (the average redshift is $z = 0.52$ without including the two $z \sim 2$ objects), supporting our conclusions that selecting objects based on fainter W4 photometry

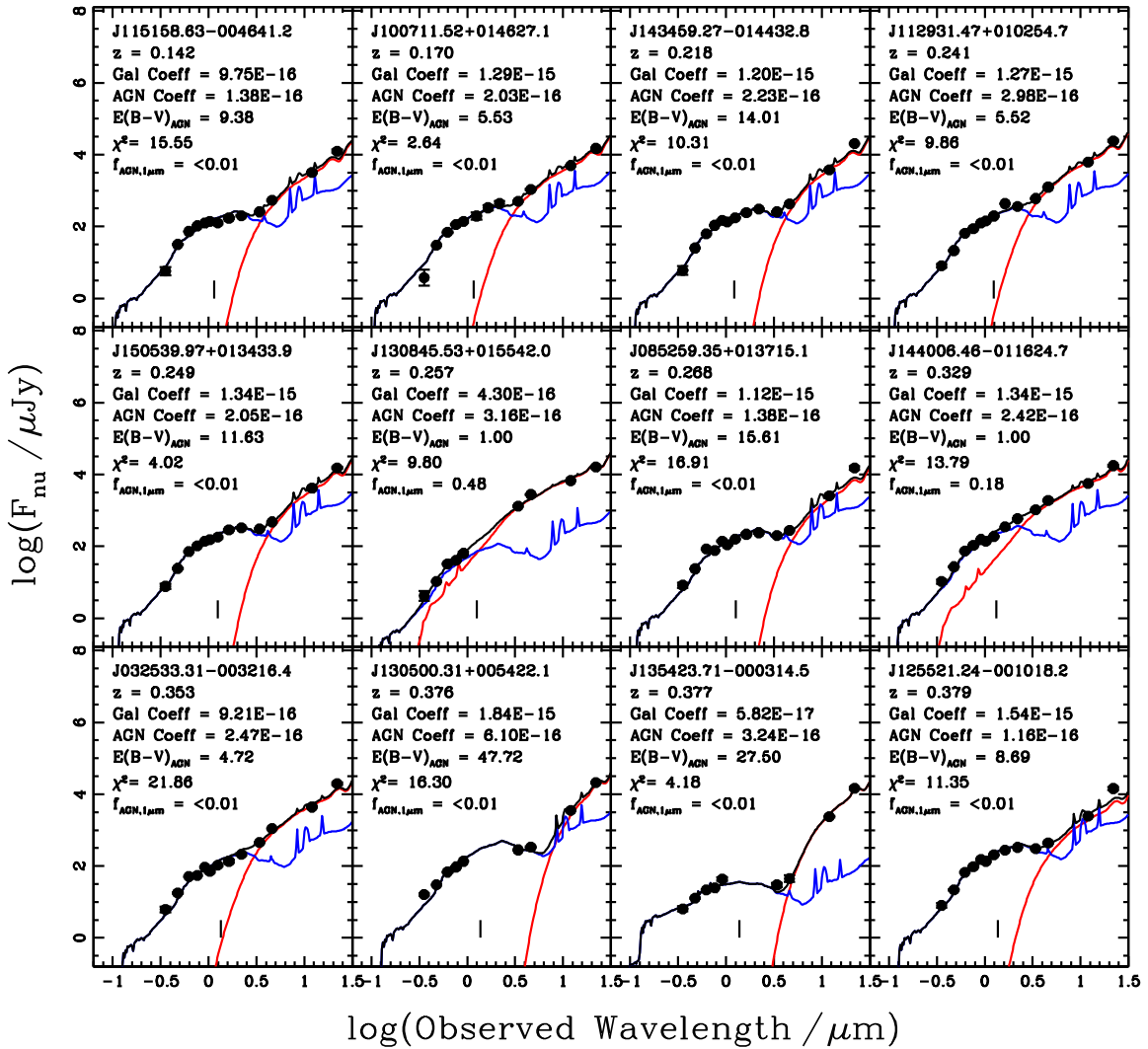


Figure 8. Best-fitting SED models for the objects in our sample with spectroscopic redshifts. We fit each object in our sample with a galaxy model (blue) combined with a dust-reddened AGN model (red), using templates from Assef et al. (2010). The fit-parameters and best-fit χ^2 are given in each panel for that specific fit. We also provide values for $f_{\text{AGN},1\mu\text{m}}$, the fraction of the total emission at rest-frame $1 \mu\text{m}$ from AGN emission derived from the fit. We show rest-frame $1 \mu\text{m}$ for each of the objects with a short vertical line below the fit. Finally, we indicate photometry that was not used for the fit with open circles.

(A color version of this figure is available in the online journal.)

leads to a higher-redshift sample. It would be of special interest to extend this photometric redshift estimation to a larger sample of SDSS+WISE-selected AGNs in order to support quasar clustering analyses (e.g., DiPompeo et al. 2014).

6. INDIVIDUAL OBJECTS

While we discussed the full population of objects in Sections 3 and 4, some of the individual objects that comprise the sample warrant a more in-depth discussion of their optical spectroscopic and SED properties. In this section, we will describe our highest-redshift sources, as well as those sources with broad emission lines in their spectra.

6.1. High-redshift Sources

Two of the objects in our sample, J0737-0052 ($z = 2.565$) and J1326-0037 ($z = 2.233$), were identified by strong UV emission lines in their observed spectrum. As discussed in Section 3, it is not surprising to find objects in our sample at these redshifts, as the redshift distribution of objects selected

to be AGNs by their WISE colors seen in many other studies commonly extends to $z \sim 2$ and above. Both of the high-redshift sources we describe have spectra with Ly α in emission, and both show evidence for C IV $\lambda 1548$ emission, while J0737-0052 also shows strong N V $\lambda 1240$ emission. These UV emission features are strongly indicative of the presence of an AGN (e.g., Hainline et al. 2011), and based on the $8 \mu\text{m}$ luminosities calculated for these objects, they are in the quasar regime.

The UV spectrum of J0737-0052 shows additional broad absorption features on each of the strong emission lines, indicating that this object is a Broad Absorption Line (BAL) quasar (Foltz et al. 1990; Weymann et al. 1991; Reichard et al. 2003; DiPompeo et al. 2012), with absorption troughs having FWHM $> 2000 \text{ km s}^{-1}$. In order to explore the broad absorption in this object, we examined the C IV $\lambda 1548$ emission and absorption profile, and we measure $\text{FWHM}_{\text{CIV}} = 2500 \text{ km s}^{-1}$. We also fit the C IV feature as a sum of Gaussians. The best fit was composed of one Gaussian in emission ($\text{FWHM} = 4080 \pm 80 \text{ km s}^{-1}$) along with two Gaussians in absorption ($\text{FWHM} = 2400 \pm 70 \text{ km s}^{-1}$ and $\text{FWHM} = 1050 \pm 70 \text{ km s}^{-1}$). While a

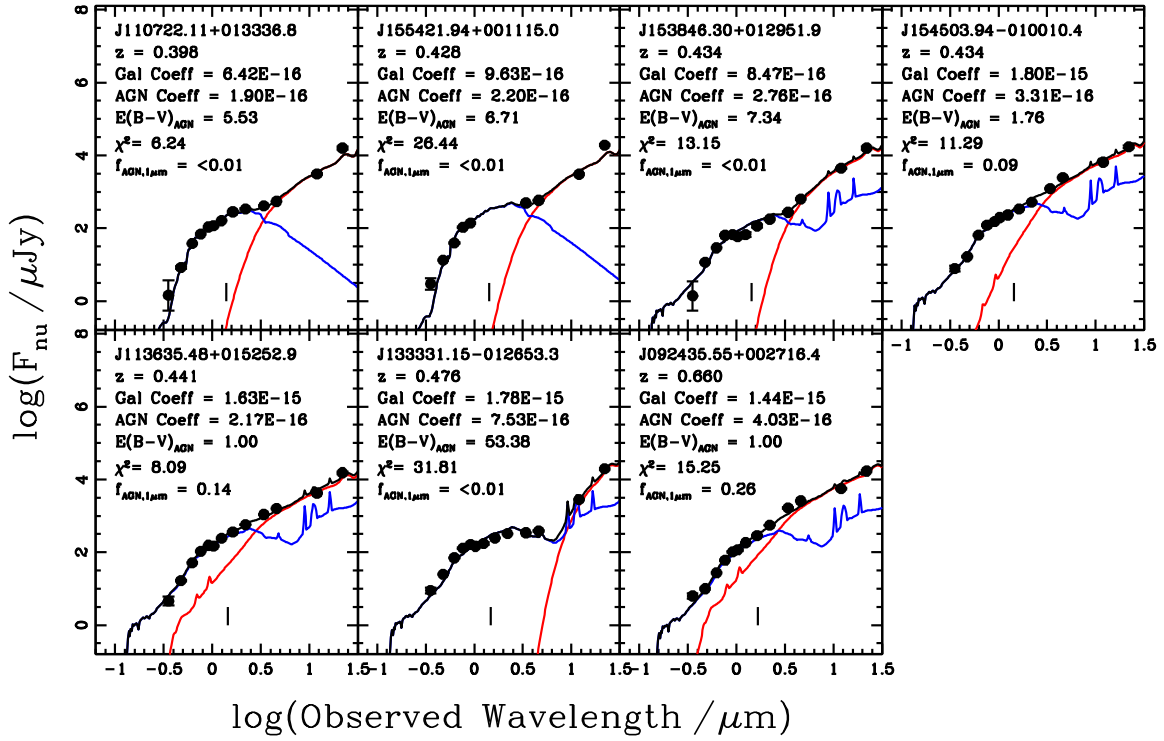


Figure 8. (Continued)

full fit of the more complex $Ly\alpha$, Nv , and $Si\,IV$ 1393+1402 regions is outside the scope of this current work, it should be noted that BAL quasars have been shown to have red optical to ultraviolet continua (Weymann et al. 1991; Sprayberry & Foltz 1992; DiPompeo et al. 2012) and the discovery of a high-redshift BAL quasar is not uncommon in other samples of optically red *WISE*-selected quasars selected under different criteria (e.g., Ross et al. 2014).

Although the spectrum of J1326–0037 does have lower S/N, we observe both the $Ly\alpha$ and $C\,IV$ $\lambda 1548$ emission lines. It is interesting to note that the $Ly\alpha$ emission line has two peaks, which may be due to intrinsic $Ly\alpha$ absorption. As we show in Figure 4, the central absorption is also seen in the two-dimensional spectrum. We fit the emission feature with two Gaussians, one in emission and the other in absorption, and found that the wavelength of the line centroids agreed with each other to within the uncertainty on the values, while the best-fit observed frame FWHM of the emission and absorption features, respectively, are $FWHM_{obs,emission} = 2500 \pm 100 \text{ km s}^{-1}$, and $FWHM_{obs,absorption} = 350 \pm 90 \text{ km s}^{-1}$. We also explored Gaussian fits under the assumption that the $Ly\alpha$ emission feature is instead double-peaked, and find that the blue peak has an observed frame $FWHM_{obs,blue} = 1500 \pm 100 \text{ km s}^{-1}$, while we measured $FWHM_{obs,red} = 730 \pm 70 \text{ km s}^{-1}$. In the rest-frame, the velocity difference between the peaks is $\Delta v_{Ly\alpha} = -1570 \pm 40 \text{ km s}^{-1}$. While the $C\,IV$ emission line also shows evidence for central absorption, the low S/N of the feature does not allow for a robust fit to determine a two-Gaussian line profile.

As seen in Figure 9 and Table 3 both of the high-redshift quasars in our sample are well fit by the AGN templates. J1326–0037 is best fit by an Im galaxy template that is dominant at short wavelengths, indicating that the UV continuum observed in the optical spectrum may be stellar in origin. As would be expected from the optical spectrum, J0737–0052 has an SED that is dominated by AGN

emission, with $f_{AGN,1\mu m} = 0.5$. Overall, both J1326–0037 and J0737–0052 represent interesting objects for potential follow-up observations.

6.2. Unobscured Sources

While our sample was selected to focus on obscured quasars, both the optical spectra and the SED modeling results demonstrate that there exists a significant number of unobscured objects. There are two objects with broad emission lines in our sample: J0737–0052 and J1634–0108. We discussed J0737–0052 in the previous section. For J1634–0108, which is unresolved in the SDSS imaging, we observe broad $Mg\,II$ $\lambda 2798$, which we fit as a sum of two Gaussians representing the narrower and a broader components of the line. The comparatively narrow component of the $Mg\,II$ emission feature for J1634–0108 is measured to have $FWHM_{Mg\,II,narrow} = 2660 \pm 60 \text{ km s}^{-1}$. For the broad component in J1634–0108, however, we measure $FWHM_{Mg\,II,broad} = 10,000 \pm 300 \text{ km s}^{-1}$. Based on the presence of these broad emission lines, we classify this object as a Type I quasar.

The remainder of our objects do not show broad emission lines in the wavelength ranged probed by our optical spectroscopy, but we can use the results from our SED modeling to demonstrate that emission at optical wavelengths likely arises from the quasar. For eight objects, we see optical emission that is dominated by quasar light: J0338–0049, J0357–0027, J0737–0052, J1320–0102, J1527–0010, J1634–0108, J1947–0036, and J2029–0108. Two of these objects are Type I quasars from their broad emission lines. The remainder are unresolved in SDSS imaging, and have low values for $E(B-V)_{AGN}$, similar to the “dust-reddened quasars” discussed in Urrutia et al. (2005), Banerji et al. (2012), and Glikman et al. (2013). Most notably, all but one of these objects (J0338–0049) have $r_{AB} - W_{2AB} > 3.1$, the demarcation we used to select obscured objects for Group 2. Some contamination of Type I objects is to be expected based

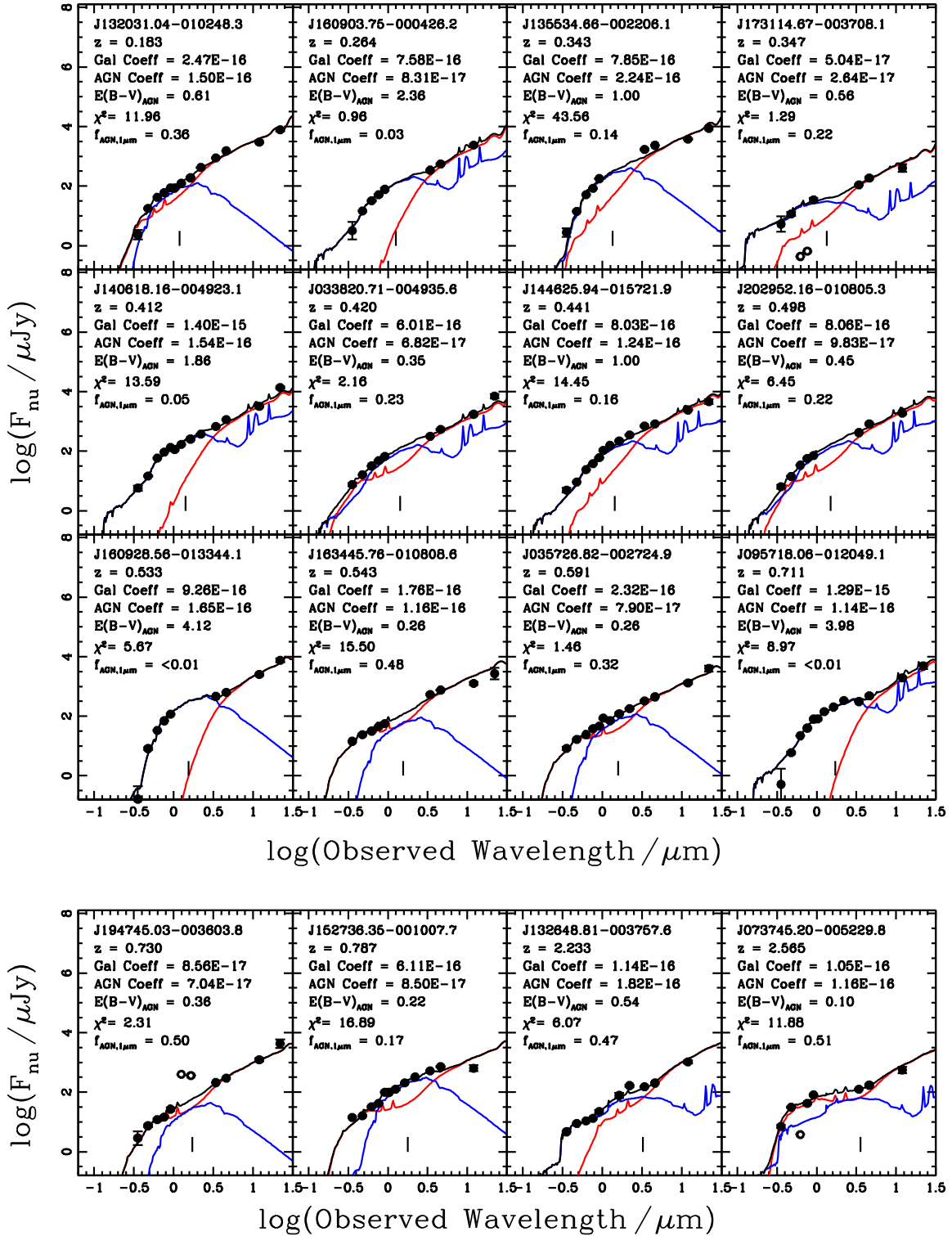


Figure 9. Best-fitting SED models for the objects in our sample with spectroscopic redshifts for Group 2. The lines and points are the same as in Figure 8.

(A color version of this figure is available in the online journal.)

on the original optical-IR selection criteria outlined in Hickox et al. (2007), and as we selected our objects in a relatively narrow range in g -band magnitude, it is likely that we are not exploring the most obscured quasars, where $g > 22$ (as discussed in Section 2, there exists a significant number of these objects that would otherwise satisfy the Group 1 and Group 2 selection criteria). There are 12 objects in our sample with $r_{\text{AB}} - W2_{\text{AB}} < 3.1$,

and of those objects, only J0338–0049 has an SED that indicates that this object is unobscured. As can be seen from our SED fits, the most obscured quasars in our sample have blue $r - W2$ colors, as the AGN only becomes dominant at longer wavelengths. Because the objects in Group 1 were chosen with bright W4 photometry and were limited to a specific range in g -band magnitude, these objects were effectively chosen using

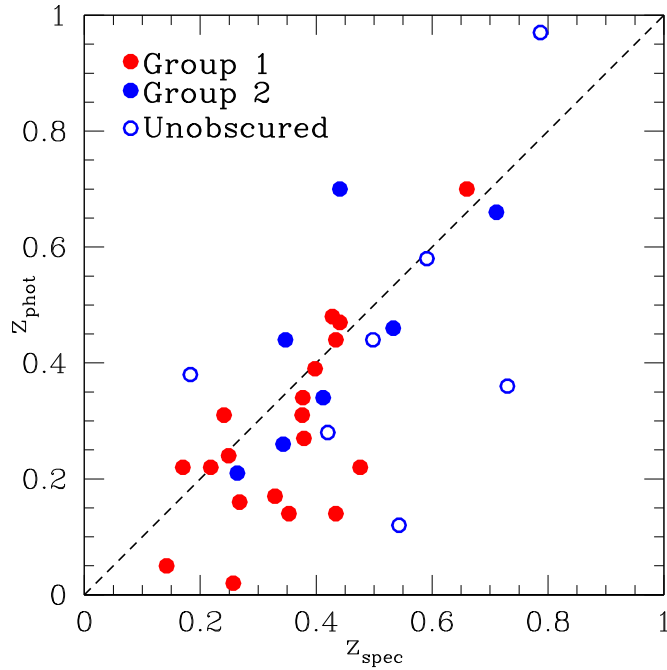


Figure 10. Spectroscopic redshift plotted against derived photometric redshift for the objects in our sample. We plot our points from Group 1 in red and Group 2 in blue, and we plot those objects with SED evidence for being unobscured with an open circle. While the majority of the objects have photometric redshifts that are similar, if slightly lower than their spectroscopic redshifts, there is a sample of AGN dominated sources which have significantly lower photometric redshifts, due to the difficulty in fitting an SED to a featureless AGN power-law SED, as seen in Figures 8–9.

(A color version of this figure is available in the online journal.)

a $g - W4$ color cut, which lead to the selection of the most heavily obscured sources in our sample.

7. COMPARISON TO OTHER AGN SELECTION CRITERIA

Based on our examination of the optical spectroscopic properties of our sample in Section 4, we conclude that the *WISE* IR selection criteria we used was largely successful at recovering obscured quasars. We compare our simple selection criteria, which was based on the $W1 - W2$ color cut from Stern et al. (2012), to other criteria discussed in the literature. Recently, Mateos et al. (2012) used AGNs selected using the Bright Ultrahard *XMM-Newton* Survey to create a *WISE* selection criteria that attempted to maximize the fraction of X-ray selected AGNs while minimizing contamination from star-forming galaxies. In a follow-up paper (Mateos et al. 2013), the authors examine the effectiveness of their revised *WISE* selection criteria in selecting obscured quasars using the SDSS Type II quasar sample described in Reyes et al. (2008). Their results indicate that it is AGN luminosity, especially with respect to host galaxy luminosity, that is the driving factor in selecting AGNs by their mid-IR colors. In this section we describe where our objects lie with respect to the Mateos et al. (2012) selection criteria.

Based solely on the selection criteria described in Mateos et al. (2012), 32/40 (80%) of the objects in our SALT spectroscopic sample fall in the Mateos et al. color-color wedge, as can be seen in Figure 1. We calculated the redshift of 28/32 (88%) of these objects, although 4 only have one emission feature in their spectrum. If we exclude objects where the redshift precludes us discerning any AGN activity in the object (due to both the wavelength coverage of the SALT chip, or either [Ne III] or [O II] falling on a chip gap or sky feature), then the Mateos et al. criteria were successful at identifying 14/17 (82%) objects with strong evidence of AGN activity based on the objects position

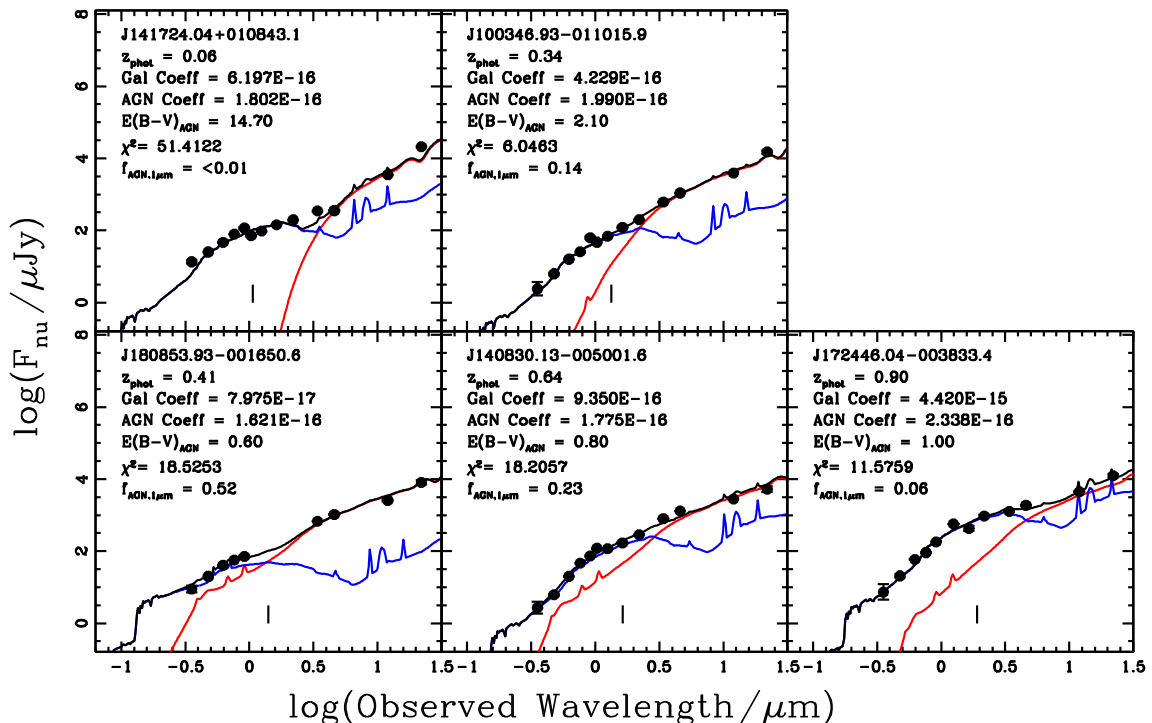


Figure 11. Best-fitting SED models for the objects in our sample without spectroscopic redshifts. The lines and points are the same as in Figure 8. The photometric redshifts are given in each plot. The top two objects are from Group 1, while the bottom three objects are from Group 2.

(A color version of this figure is available in the online journal.)

on the TBT diagram, the BPT diagram, or the presence of high-ionization emission lines in the UV spectrum for the two highest-redshift objects. The other three objects have upper limits on the $[\text{Ne III}]/[\text{O II}]$ ratio, indicating a non-detection of $[\text{Ne III}]$ in the spectrum.

Eight objects in our SALT sample would not be selected under the Mateos et al. (2012) criteria. Two of these objects have unusual $W2-W3$ colors, J1527-0010 ($W2 - W3 = 1.80$), and J1354-0003 ($W2 - W3 = 6.24$). There is only one emission line identified in the spectrum of J1527-0010 and while J1354-0003 is in the AGN region of the TBT diagram, the position of this object is in the region also occupied by AGN/SF composite objects.

The other six objects not selected by the Mateos et al. (2012) wedge have red $W2-W3$ colors that put them below and to the right of the wedge. Five of these objects (J1305+0054, J0852+0137, J1554+0011, J1107+0133, and J1333-0126) are identified as AGNs based on their position on the TBT diagram, and we have not identified the spectroscopic redshift of the sixth object, J1417+0108. The presence of AGNs outside of the Mateos et al. (2012) selection region is not surprising; these authors used an analysis of AGN mid-IR templates to demonstrate that heavily obscured AGNs, as well as higher-redshift AGNs ($z \sim 1-1.5$) would occupy this position in *WISE* color-color space. The positions of heavily obscured AGNs in *WISE* color-color space was further discussed in Mateos et al. (2013), where the relative contribution of an AGN and its host to the mid-IR SED was the primary factor that determines whether or not an AGN was found in the Mateos et al. selection wedge. For the five objects in our sample outside the wedge with spectroscopic redshifts, the best-fit SEDs indicate that these objects have a best-fit value of $E(B - V)_{\text{AGN}} > 6.0$ (three of these objects have $E(B - V)_{\text{AGN}} > 16.9$), indicating that the AGN only becomes dominant in the mid-IR; this is expected based on the red $W2-W3$ colors for these objects. As mentioned in the previous section, these objects would not be chosen under the Group 2 selection criteria, as they have $r_{\text{AB}} - W2_{\text{AB}} < 3.1$. For selecting the most highly obscured quasars, these results indicate the necessity in using an optical to infrared color cut with the $W3$ or $W4$ photometric bands. These high values for $E(B - V)$ indicate that these objects are likely obscured quasars, but it should be noted that while we do apply a simple prescription for obscuration in our SED fitting, we do not know the geometry of the obscuring medium. As we do see strong infrared emission, we know that there must be dust near the central black hole, but galaxy-scale dust can also contribute to the observed obscuration (see Merloni et al. 2014; Chen et al. 2014). We cannot rule out extreme SF as the origin of the rest-frame IR photometry, supported by the measurement of $f_{\text{AGN}, 1\mu\text{m}} \leq 0.01$ for these objects and the position of the Polletta et al. (2007) Arp220 template occupying a similar position on the color-color diagram at low redshift as can be seen in Figure 1. However, this figure as well as Mateos et al. (2013) demonstrate that a significant number of SDSS Type II quasars from the Reyes et al. (2008) sample also fall into this region and would not be selected as IR-AGNs using the Mateos et al. (2012) criteria.

We can also use the SED modeling results to test whether our full sample of objects would be selected under the *Spitzer* selection criteria outlined in Lacy et al. (2004), Stern et al. (2005), and Donley et al. (2012). We passed the best-fit combined stellar and AGN template through the *Spitzer* IRAC transmission curves to estimate *Spitzer* photometry. We find that

all objects but one fall into the Lacy et al. (2004) selection box. The lone outlier, J1354-0003, has an SED with a very strong AGN power law as compared to the stellar population, as seen in Figure 8. Donley et al. (2012) revised the Lacy et al. (2004) criteria in order to account for contamination to the IR from star-forming galaxies, and we find that only three of our targets would lie outside of the Donley et al. (2012) selection box. These objects, J1333-0126, J1305+0054 and J0852+0137, are objects that would also not be selected under the Mateos et al. (2012) criteria and have near-IR emission dominated by host galaxy light, with our SED modeling showing that an AGN contribution is only prominent at longer wavelengths. The bulk of the targets that comprise our sample, then, compare very well to the *Spitzer*-selected objects described in Lacy et al. (2013).

8. CONCLUSIONS

The all-sky coverage of *WISE* has made it possible to find large numbers of obscured quasars based solely on their observed infrared colors. We have observed a sample of 40 objects with *WISE* colors indicative of AGN activity in two groups. Group 1 objects were initially selected to have $W1 - W2 > 0.7$ and $7 \geq W4 \geq 6.5$, while Group 2 objects were initially selected to have $W1 - W2 > 0.8$, $W4 \geq 7.0$, and $r_{\text{AB}} - W2_{\text{AB}} > 3.1$. Both groups were selected to have $20 < g < 22$. We used optical spectroscopy from SALT RSS to uncover the redshift distribution and ionization properties of obscured quasars. We use the ratio $[\text{O III}]/\text{H}\beta$, and $[\text{Ne III}]/[\text{O II}]$ to determine that the majority of our objects in our sample are AGNs: of those objects with redshifts that allow us to use emission lines to identify the ionization source, only $\sim 13\%$ of the objects in our sample do not have evidence in their observed spectra of being an AGN. For the AGNs, we measure $[\text{O III}]$ and IR luminosities that are comparable to SDSS-selected quasars. The objects in our sample have an average redshift of $z \sim 0.5$, and the majority have $z < 1.0$, which is most likely a result of our optical photometric cut. Our sample also includes two interesting high-redshift sources, a BAL quasar at $z = 2.565$, and a quasar with $\text{Ly}\alpha$ and $\text{C IV } \lambda 1549$ emission at $z = 2.233$.

We also use a simple two-component SED analysis to explore the relationship between AGN and SF as a function of the position of the objects on the *WISE* $W1-W2$ versus $W3-W4$ color-color diagram. The majority of the objects in our sample have strong AGN emission in the mid-IR. We also compared our selection criteria to that of Mateos et al. (2012). While their criteria are successful at recovering the AGNs in our sample, there are five objects outside of their selection wedge at red $W3-W4$ colors with optical line ratios indicative of AGN activity. SED modeling of these objects demonstrates that these are the most highly obscured quasars in our sample, in line with the conclusions made in Mateos et al. (2012). These results indicate the selecting objects based on red optical to $W3$ or $W4$ colors is required to select objects with the highest levels of obscuration.

The results from observing and analyzing this small sample of obscured quasars are currently being used to understand the entire population of obscured quasars with both *WISE* and SDSS photometry. We can use our results from the photometric redshift estimation for these objects to aid future *WISE*-selected AGN clustering studies. The most heavily obscured quasars in our sample (such as J1354-0003, with a strong AGN component to the SED that only becomes apparent at the longest mid-IR wavelengths) may also be excellent targets for observations in the hard X-ray portion of the spectrum with The Nuclear

Spectroscopic Telescope Array (*NuSTAR*) High-energy X-Ray telescope (Harrison et al. 2013). We are also using SALT to probe portions of the *WISE* $W1-W2$ versus $W2-W3$ color-color diagram that are not spanned by our current sample. Together, our results along with future analysis help demonstrate the power of mid-IR *WISE* selection for recovering large samples of obscured quasars.

We acknowledge the referee for a constructive report which significantly improved the paper. K.N.H., R.C.H., A.D.M., and M.A.D. were partially supported by NASA through ADAP award NNX12AE38G and by the National Science Foundation through grant numbers 1211096 and 1211112.

Some of the observations reported in this paper were obtained with the Southern African Large Telescope (SALT). This publication also makes use of data products from the *Wide-field Infrared Survey Explorer*, which is a joint project of the University of California, Los Angeles, and the Jet Propulsion Laboratory/California Institute of Technology, funded by the National Aeronautics and Space Administration. Funding for SDSS-III has been provided by the Alfred P. Sloan Foundation, the Participating Institutions, the National Science Foundation, and the U.S. Department of Energy Office of Science. The SDSS-III Web site is <http://www.sdss3.org/>.

SDSS-III is managed by the Astrophysical Research Consortium for the Participating Institutions of the SDSS-III Collaboration including the University of Arizona, the Brazilian Participation Group, Brookhaven National Laboratory, Carnegie Mellon University, University of Florida, the French Participation Group, the German Participation Group, Harvard University, the Instituto de Astrofísica de Canarias, the Michigan State/Notre Dame/JINA Participation Group, Johns Hopkins University, Lawrence Berkeley National Laboratory, Max Planck Institute for Astrophysics, Max Planck Institute for Extraterrestrial Physics, New Mexico State University, New York University, Ohio State University, Pennsylvania State University, University of Portsmouth, Princeton University, the Spanish Participation Group, University of Tokyo, University of Utah, Vanderbilt University, University of Virginia, University of Washington, and Yale University.

REFERENCES

- Ahn, C. P., Alexandroff, R., Allende Prieto, C., et al. 2012, *ApJS*, **203**, 21
- Aihara, H., Allende Prieto, C., An, D., et al. 2011, *ApJS*, **193**, 29
- Alexander, D. M., Bauer, F. E., Brandt, W. N., et al. 2003, *AJ*, **125**, 383
- Alexander, D. M., Chary, R.-R., Pope, A., et al. 2008, *ApJ*, **687**, 835
- Alexander, D. M., & Hickox, R. C. 2012, *NewAR*, **56**, 93
- Antonucci, R. 1993, *ARA&A*, **31**, 473
- Ashby, M. L. N., Stern, D., Brodwin, M., et al. 2009, *ApJ*, **701**, 428
- Assef, R. J., Kochanek, C. S., Brodwin, M., et al. 2010, *ApJ*, **713**, 970
- Assef, R. J., Stern, D., Kochanek, C. S., et al. 2013, *ApJ*, **772**, 26
- Baldwin, J. A., Phillips, M. M., & Terlevich, R. 1981, *PASP*, **93**, 5
- Ballantyne, D. R., Draper, A. R., Madsen, K. K., Rigby, J. R., & Treister, E. 2011, *ApJ*, **736**, 56
- Banerji, M., McMahon, R. G., Hewett, P. C., et al. 2012, *MNRAS*, **427**, 2275
- Becker, R. H., White, R. L., & Helfand, D. J. 1995, *ApJ*, **450**, 559
- Blanton, M. R., & Roweis, S. 2007, *AJ*, **133**, 734
- Brandt, W. N., & Alexander, D. M. 2010, *PNAS*, **107**, 7184
- Brodwin, M., Brown, M. J. I., Ashby, M. L. N., et al. 2006, *ApJ*, **651**, 791
- Burlon, D., Ajello, M., Greiner, J., et al. 2011, *ApJ*, **728**, 58
- Cardelli, J. A., Clayton, G. C., & Mathis, J. S. 1989, *ApJ*, **345**, 245
- Chary, R., & Elbaz, D. 2001, *ApJ*, **556**, 562
- Chen, C.-T. J., Hickox, R. C., Alberts, S., et al. 2014, *ApJ*, submitted
- Chung, S. M., Kochanek, C. S., Assef, R., et al. 2014, *ApJ*, **790**, 54
- Comastri, A., Setti, G., Zamorani, G., & Hasinger, G. 1995, *A&A*, **296**, 1
- Cutri, R. M., Wright, E. L., Conrow, T., et al. 2013, Explanatory Supplement to the AllWISE Data Release Products, Tech. rep.
- Cutri, R. M. e. 2013, *yCat*, **2328**, 0
- DiPompeo, M. A., Brotherton, M. S., Cales, S. L., & Runnoe, J. C. 2012, *MNRAS*, **427**, 1135
- DiPompeo, M. A., Myers, A. D., Hickox, R. C., Geach, J. E., & Hainline, K. N. 2014, *MNRAS*, **442**, 3443
- Donley, J. L., Koekemoer, A. M., Brusa, M., et al. 2012, *ApJ*, **748**, 142
- Donley, J. L., Rieke, G. H., Pérez-González, P. G., & Barro, G. 2008, *ApJ*, **687**, 111
- Donoso, E., Yan, L., Stern, D., & Assef, R. J. 2014, *ApJ*, **789**, 44
- Fabian, A. C. 2012, *ARA&A*, **50**, 455
- Foltz, C. B., Chaffee, F. H., Hewett, P. C., Weymann, R. J., & Morris, S. L. 1990, *BAAS*, **22**, 806
- Gilli, R., Comastri, A., & Hasinger, G. 2007, *A&A*, **463**, 79
- Glikman, E., Urrutia, T., Lacy, M., et al. 2013, *ApJ*, **778**, 127
- Gordon, K. D., & Clayton, G. C. 1998, *ApJ*, **500**, 816
- Hainline, K. N., Hickox, R., Greene, J. E., Myers, A. D., & Zakamska, N. L. 2013, *ApJ*, **774**, 145
- Hainline, K. N., Shapley, A. E., Greene, J. E., et al. 2012, *ApJ*, **760**, 74
- Hainline, K. N., Shapley, A. E., Greene, J. E., & Steidel, C. C. 2011, *ApJ*, **733**, 31
- Harrison, F. A., Craig, W. W., Christensen, F. E., et al. 2013, *ApJ*, **770**, 103
- Hewett, P. C., Warren, S. J., Leggett, S. K., & Hodgkin, S. T. 2006, *MNRAS*, **367**, 454
- Hickox, R. C., Jones, C., Forman, W. R., et al. 2007, *ApJ*, **671**, 1365
- Hopkins, P. F., Hernquist, L., Cox, T. J., et al. 2006, *ApJS*, **163**, 1
- Hopkins, P. F., Hernquist, L., Cox, T. J., & Kereš, D. 2008, *ApJS*, **175**, 356
- Hopkins, P. F., Richards, G. T., & Hernquist, L. 2007, *ApJ*, **654**, 731
- Ivezić, Ž., Menou, K., Knapp, G. R., et al. 2002, *AJ*, **124**, 2364
- Jarrett, T. H., Cohen, M., Masci, F., et al. 2011, *ApJ*, **735**, 112
- Kauffmann, G., & Haehnelt, M. 2000, *MNRAS*, **311**, 576
- Kauffmann, G., Heckman, T. M., Tremonti, C., et al. 2003, *MNRAS*, **346**, 1055
- Kennicutt, R. C. 1998, *ARA&A*, **36**, 189
- Kewley, L. J., Groves, B., Kauffmann, G., & Heckman, T. 2006, *MNRAS*, **372**, 961
- Kobulnicky, H. A., Willmer, C. N. A., Phillips, A. C., et al. 2003, *ApJ*, **599**, 1006
- Komatsu, E., Smith, K. M., Dunkley, J., et al. 2011, *ApJS*, **192**, 18
- Lacy, M., Ridgway, S. E., Gates, E. L., et al. 2013, *ApJS*, **208**, 24
- Lacy, M., Storrie-Lombardi, L. J., Sajina, A., et al. 2004, *ApJS*, **154**, 166
- Lawrence, A., Warren, S. J., Almaini, O., et al. 2007, *MNRAS*, **379**, 1599
- Mainieri, V., Bergeron, J., Hasinger, G., et al. 2002, *A&A*, **393**, 425
- Mainieri, V., Bongiorno, A., Merloni, A., et al. 2011, *A&A*, **535**, A80
- Mateos, S., Alonso-Herrero, A., Carrera, F. J., et al. 2012, *MNRAS*, **426**, 3271
- Mateos, S., Alonso-Herrero, A., Carrera, F. J., et al. 2013, *MNRAS*, **434**, 941
- Mateos, S., Barcons, X., Carrera, F. J., et al. 2005, *A&A*, **444**, 79
- Mendez, A. J., Coil, A. L., Aird, J., et al. 2013, *ApJ*, **770**, 40
- Merloni, A., Bongiorno, A., Brusa, M., et al. 2014, *MNRAS*, **437**, 3550
- Oyaizu, H., Lima, M., Cunha, C. E., et al. 2008, *ApJ*, **674**, 768
- Polletta, M., Tajer, M., Maraschi, L., et al. 2007, *ApJ*, **663**, 81
- Reichard, T. A., Richards, G. T., Schneider, D. P., et al. 2003, *AJ*, **125**, 1711
- Reyes, R., Zakamska, N. L., Strauss, M. A., et al. 2008, *AJ*, **136**, 2373
- Ross, N. P., Hamann, F., Zakamska, N. L., et al. 2014, *arXiv:1405.1047*
- Salvato, M., Ilbert, O., Hasinger, G., et al. 2011, *ApJ*, **742**, 61
- Salvato, M., Hasinger, G., Ilbert, O., et al. 2009, *ApJ*, **690**, 1250
- Shen, Y., Richards, G. T., Strauss, M. A., et al. 2011, *ApJS*, **194**, 45
- Shi, Y., Helou, G., & Armus, L. 2013, *ApJ*, **777**, 6
- Skrutskie, M. F., Cutri, R. M., Stiening, R., et al. 2006, *AJ*, **131**, 1163
- Smith, M. P., Nordsieck, K. H., Burgh, E. B., et al. 2006, *Proc. SPIE*, **6269**, 62692A
- Sprayberry, D., & Foltz, C. B. 1992, *ApJ*, **390**, 39
- Stern, D., Assef, R. J., Benford, D. J., et al. 2012, *ApJ*, **753**, 30
- Stern, D., Eisenhardt, P., Gorjian, V., et al. 2005, *ApJ*, **631**, 163
- Tozzi, P., Gilli, R., Mainieri, V., et al. 2006, *A&A*, **451**, 457
- Treister, E., Urry, C. M., & Virani, S. 2009, *ApJ*, **696**, 110
- Trouille, L., Barger, A. J., & Tremonti, C. 2011, *ApJ*, **742**, 46
- Urrutia, T., Lacy, M., Gregg, M. D., & Becker, R. H. 2005, *ApJ*, **627**, 75
- Urry, C. M., & Padovani, P. 1995, *PASP*, **107**, 803
- Weymann, R. J., Morris, S. L., Foltz, C. B., & Hewett, P. C. 1991, *ApJ*, **373**, 23
- Worsley, M. A., Fabian, A. C., Bauer, F. E., et al. 2005, *MNRAS*, **357**, 1281
- Wright, E. L., Eisenhardt, P. R. M., Mainzer, A. K., et al. 2010, *AJ*, **140**, 1868
- Xue, Y. Q., Brandt, W. N., Luo, B., et al. 2011, in ASP Conf. Ser. 439, The Galactic Center: A Window to the Nuclear Environment of Disk Galaxies, ed. M. R. Morris, Q. D. Wang, & F. Yuan (San Francisco, CA: ASP), 478